Workshop of

Experimental Nuclear and Particle Physics

2018

14.–20. 01. 2018, Bílý Potok

Faculty of Nuclear Sciences and Physical Engineering
Czech Technical University in Prague

Workshop of Experimental Nuclear and Particle Physics 2018
Editors: L. Novotný, R. Novotný
Issued by: Czech Technical University in Prague
Faculty of Nuclear Sciences and Physical Engineering
Address: KF FJFI ČVUT, Břehová 7, 115 19 Praha 1
novotr14@fjfi.cvut.cz, +420731891801
Available at http://wejcf2018.ejcf.cz/wejcf2018_proceedings.pdf
First edition. 81 pages.

Contents

Foreword

This year, for the 12^{th} time, students, graduates, and teachers from the field of Experimental Nuclear and Particle Physics at FNSPE CTU met at the annual winter workshop. The meeting was held during the week of 14.–20. 01. 2018 at *Penzion Krakonoš* in the Jizera Mountains in the Czech Republic. The main goal of the workshop is to follow the progress of students, discuss problems and experiences and also to get to know each other better. Each participant gave a talk about their work or progress during the previous year. Extended abstracts of these talks are published in the proceedings you are holding now.

Editors

Practical use of quantum entanglement

Elisabeth Andriantsarazo*(andrieli@fjfi.cvut.cz)*

In this proceedings we discuss advantages of an interesting quantum feature called entanglement and how to possibly profit from it in the future. We introduce the entanglement itself and how to employ it in a field called quantum cryptography. We also present one cryptographic protocol, which directly uses the entanglement.

1 Quantum entanglement

Suppose we have a state $|\psi\rangle_{AB}$ made out of two subsystems A and B. Their states are described as follows: $|\phi\rangle_A$ and $|\varphi\rangle_B$. The system $|\psi\rangle_{AB}$ is called entangled if the following is true:

$$|\psi\rangle_{AB} \neq |\phi\rangle_A \otimes |\varphi\rangle_B \,. \tag{1}$$

Such state is by definition unseparable and the two subsystems A,B have no eigenstates themselves. Entanglement has always been a confusing property that has no classical counterpart. It violates the local realist view of causality and it brought many people, such as Einstein, to doubt correctness of quantum mechanics. Further reading can be found here [1].

Let us define a a quantum bit (shortly qubit), which is an analogue of the classical bit in quantum information theory. System of a qubit can be written as follows: $|\psi\rangle = a\,|0\rangle + b\,|1\rangle$ $a, b \in \mathbb{R}$. As we see it is a superposition of two states, $|0\rangle$ and $|1\rangle$. Qubit can be mathematically represented as a unit vector in twodimensional Hilbert space and realized, in a lab, by a photon in one of two polarization states, vertical $|V\rangle$ or horizontal $|H\rangle$. Entangled photons are usually produced in a nonlinear optical effect called spontaneous parametric downconversion (SPDC shortly). In this process one photon, called pump, enters a nonlinear optic material and is split into a photon pair with correlated poralization states.

Entanglement can be also used in a device called quantum computer, which should, supposedly, have much larger computing power that supercomputers used today. Qubits in such device are interfering and entangled, the computer uses all qubits at once. This should increase the computing power and make some of the cryptography protocols used today, such as RSA protocol, obsolete.

2 Quantum cryptography

Quantum cryptography concentrates mostly on quantum key distribution. Safety is guaranteed by principles of quantum measurement, as we can detect and find out if someone is trying to eavesdrop.

2.1 Ekert protocol

Let us shortly introduce on of the well-known quantum protocols called Ekert protokol, see figure **??**. In this protocol we use a source of entangled photons, each of them representing a qubit. Suppose we have two people, Alice and Bob, that want to share a key. First they share n qubits in following state:

$$|\psi\rangle = \frac{1}{\sqrt{2}}(|00\rangle + |11\rangle). \tag{2}$$

Left side belongs to Alice, right side to Bob, each of them has acces one qubit. After that they independently generate a pair of random number (a, a') $\in \{0, 1\}$. Each number defines basis in which a qubit is measured. They get an output (b, b'), which they share with each other, and if b = b' they accept the pair (a, a'), hence a bit in a corellated random key was established.

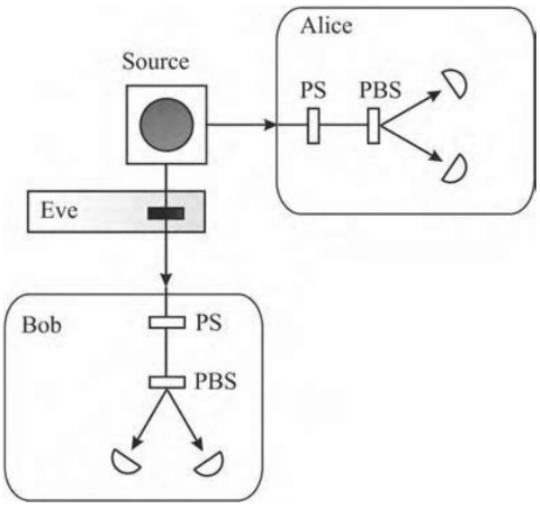

Figure 1: Scheme of the Ekert protocol. Source creates entangled photons which Alice and Bob recieves, source [2].

Let's say there is a person, called Eve, that wants to uncover the key and steal it. If she tries to detect and measure the qubit, she will, by definition, change the state of the system. Corellation between entangled photons is then broken and those two photons start satisfying Bell inequalities. This way we know which qubit should not be used in the key and it should be impossible for a third party to eavesdrop without detection.

References

[1] A. Einstein,B. Podolsky, R. Nathan, Phys. Review 47(10), 777 (1935)

[2] M. Nielsen, I. Chuang, Quantum computation and quantum information, (2002)

Connection between Energy Spectrum, Mass Composition and Distribution of Sources of Extragalactic Cosmic Rays

Alena Bakalová *(bakalale@fjfi.cvut.cz)*

Cosmic rays are charged particles that come from outer space. Since these particles are deflected by the Lorentz force in cosmic magnetic fields during the propagation in the Universe, their arrival direction does not need to point to the source of their origin. For particles with lower energies ($< 10^{17}$ eV) the galactic magnetic field is so strong that they become confined within the galaxy, while for higher energies, the Larmor radius becomes larger and particles can escape from the galaxy [1]. Ultra high energy cosmic rays (UHECR) are of extragalactic origin [2], therefore they are deflected by both galactic and extragalactic magnetic fields. While the strength of galactic magnetic fields (GMF) can be estimated from multiple measurements, the origin and strength of extragalactic magnetic fields (EGMF) is still not well understood.

Recent measurements by the Pierre Auger Observatory found a large scale anisotropy in the arrival directions of UHECR with energies above $8 \cdot 10^{18}$ eV [2]. This anisotropy is in the form of a dipole in right ascension as is depicted in Figure 1. Alongside with this measurement a conclusion was made that if an anisotropy is be observed at Earth for UHECR, the distribution of cosmic rays must be anisotropic outside of the Galaxy and that it can not be produced by deflections in magnetic field.

In order to verify such a conclusion we performed simulations of cosmic ray propagation in the GMF. CRPropa code [3] was used to propagate cosmic-ray particles in the Jansson and Farrar 2012 model of GMF (JF12) [4, 5]. Protons were sent isotropically from a sphere of a radius 20 kpc, which should approximately correspond to the Milky Way radius. The observer was placed to the Cartesian coordinates (-8.5, 0, 0) kpc, which is the rough estimate of the Solar System location. Simulated protons followed a power law energy spectrum with spectral index $\gamma = -3$ with energies $(8 - 100) \cdot 10^{18}$ eV. In these simulations the energy losses of particles were neglected since the energy loss lengths are rather in orders of Mpc. Due to the high computational time, the observer was taken as a sphere of a radius of 100 pc. Resulting distribution of normalized rates as a function of right ascension on the observer is shown in Figure 2. It is clearly visible that the distribution is not isotropic and also follows rather a dipole anisotropy.

Our results demonstrate that an anisotropy observed on Earth actually might arise even from an isotropic flux of cosmic rays to the galaxy and this anisotropy is certainly a result of the galactic magnetic field. In our further research we will continue to investigate

this phenomenon for different primary particles and we will attempt to reduce the observer radius as well as perform the simulations for a different model of GMF.

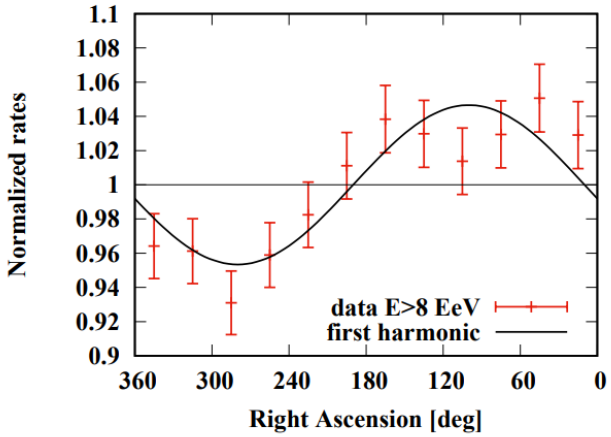

Figure 1: Normalized rate of measured events by the Pierre Auger Observatory as a function of right ascension [2].

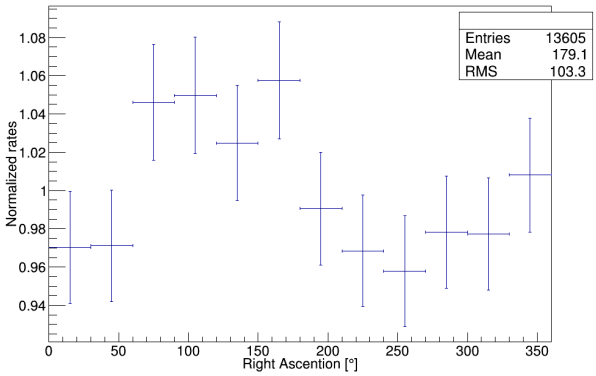

Figure 2: Normalized rate of simulated particles in CRPropa as a function of right ascension on the observer from isotropic distribution of the initial arrival directions entering the Galaxy.

References

[1] S. Hackstein et al., Monthly Notices of the Royal Astronomical Society 462, 3660-3671 (2016)

[2] The Pierre Auger Collaboration, Science 357, 1266-1270 (2017)

[3] R. A. Batista et al., Journal of Cosmology and Astroparticle Physics 1605, 038 (2016)

[4] R. Jansson, G. R. Farrar, Astrophysical Journal 757, 14 (2012)

[5] R. Jansson, G. R. Farrar, Astrophysical Journal 761, L11 (2012)

Numerical solutions to the Balitsky-Kovchegov evolution equation

Dagmar Bendová *(Dagmar.Bendova@fjfi.cvut.cz)*

1 Introduction

The proton is composed of partons which are identified with quarks and gluons. The partons are bound in the proton by the strong force described by the means of Quantum Chromodynamics. At small energies most of the momentum p of the proton is carried by valence quarks. However the composition changes with increasing energy, i.e. with acceleration of the proton. This change is called QCD evolution of the partonic structure of the proton and proceeds in two ways. Considering the evolution in the scale of the process Q^2, more "smaller" partons appear with increasing energy. If we observe the evolution in rapidity $Y = \ln(\frac{1}{x})$, where x is the Bjorken variable, each parton radiates more "same" partons. This leads to non-linear evolution of the proton structure. Phase space of the proton is filled with partons and therefore its wave functions start to overlap which causes the recombination of partons. Eventually a balance called parton saturation is reached. It is possible to examine this behavior in Deep Inelastic Scattering in which electron radiates virtual photon which can subsequently fluctuate into $q\bar{q}$ dipole. A parton from the proton than interacts strongly with the dipole and after that, the dipole collapses back to virtual photon. The cross-section of the dipole interacting with hadron tagret can be obtained from the dipole scattering amplitude $N(x, r)$. The evolution with rapidity Y of the scattering amplitude $N(x, r)$ of a $q\bar{q}$ dipole with the hadronic target is described by the Balitsky-Kovchegov evolution equation.

2 Numerical solution to rcBK equation

The Balistky-Kobchegov evolution equation with running coupling kernel [1] reads

$$\frac{\partial N(r,Y)}{\partial Y} = \int \mathrm{d}\vec{r_1} K(\vec{r},\vec{r_1},\vec{r_2}) \left[N(r_1,Y) + N(r_2,Y) - N(r,Y) - N(r_1,Y)N(r_2,Y)\right], \quad (1)$$

where the kernel $K(\vec{r},\vec{r_1},\vec{r_2})$ can be expressed as [2]

$$K(\vec{r},\vec{r_1},\vec{r_2}) = \frac{\alpha_S(r^2)N_C}{2\pi^2}\left(\frac{r^2}{r_1^2 r_2^2} + \frac{1}{r_1^2}\left(\frac{\alpha_S(r_1^2)}{\alpha_S(r_2^2)} - 1\right) + \frac{1}{r_2^2}\left(\frac{\alpha_S(r_2^2)}{\alpha_S(r_1^2)} - 1\right)\right). \quad (2)$$

The running coupling constant is calculated as

$$\alpha_S(r^2) = \frac{4\pi}{\beta_{0,n_f} \ln\left(\frac{4C^2}{r^2\Lambda_{QCD}}\right)}, \qquad \beta_{0,n_f} = \left(11 - \frac{2}{3}n_f\right). \tag{3}$$

As the (1) is an integro-differential equation one needs an appropriate initial condition to solve it. We use the initial form of the scattering amplitude from McLearran-Venugopalan model

$$N(r, Y = 0) = 1 - \exp\left(-\frac{(r^2 Q_{s0}^2)^\gamma}{4} \ln\left(\frac{1}{r\Lambda_{QCD}} + e\right)\right) \tag{4}$$

with parameters $Q_{s0}^2 = 0.165$ GeV^2, $\gamma = 1.135$ and $C = 2.52$, which were taken from fit [2], $n_f = 3$ and $\Lambda_{QCD} = 0.241$ MeV is set according to [1]. Optionaly one may incorporate also the contribution from heavy quarks for the choice of $n_f = 4$ or $n_f = 5$. In this case the values of Λ_{QCD} depend on the number of active flavours and are determined from the experimentally measured values of α_S at Z^0 mass

$$\Lambda_5 = M_Z \exp\left(-\frac{2\pi}{\alpha_S(M_Z)\beta_5}\right) \tag{5}$$

$$\Lambda_{n_{f-1}} = (m_f)^{1-\frac{\beta_{0,n_f}}{\beta_{0,n_{f-1}}}} \left(\Lambda_{n_f}\right)^{\frac{\beta_{0,n_f}}{\beta_{0,n_{f-1}}}} \tag{6}$$

with matching condition for the running coupling at the scale $r_*^2 = \frac{4C^2}{m_f^2}$

$$\alpha_{S,n_{f-1}}(r_*^2) = \alpha_{S,n_f}(r_*^2) \tag{7}$$

The rcBK equation (1) is solved using Runge-Kutta methods of the 1$^{\text{st}}$, 2$^{\text{nd}}$ and 4$^{\text{th}}$ order [1] over a grid in r which is the transverse size of the dipole. All the definite integrals appearing in RK methods are solved using Simpson's method. We chose a step in rapidity size $\Delta Y = 0.05$ and a grid in r of the size of 1000 points which are spaced uniformly in $\log_{10}(r)$ from $r_{min} = 10^{-7}$ GeV^{-1} to $r_{max} = 10^2$ GeV^{-1}.

3 Results

We compared the three RK methods used for the solution of rcBK equation. The comparison can be seen in Figure 1. As can be seen, the difference between the RK method of the 1$^{\text{st}}$ order and other two methods are approx. 1 % and there is no observable difference between the result of RK method of the 2$^{\text{nd}}$ and 4$^{\text{th}}$ order.
In Figure 2 we can see the comparison of the various choice of number of active flavours. As is apparent the contribution from heavy quarks is larger with increasing Y.

4 Conclusion

The procedure for the numerical solution of the rcBK equation (1) with kernel (2) for McLerran-Venugopalan initial condition was obtained. We implemented three Runge-Kutta methods and compared them. Also the contribution from the heavy quarks was incorporated within the so called variable flavour scheme which enables the optional choice of number of active flavours n_f and therefore the running coupling constant (3) is calculated at appropriate scale.

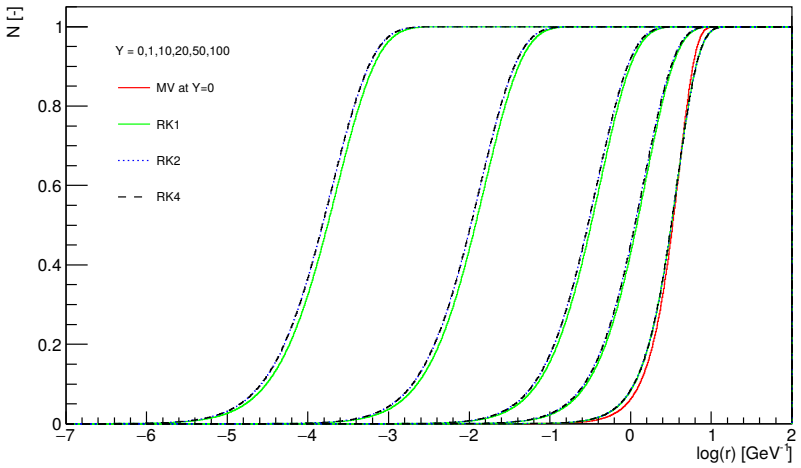

Figure 1: Evolution of the scattering amplitude $N(r, Y)$ of a $q\bar{q}$ dipole with a hadronic target up to rapidity $Y = 100$ for RK methods of 1$^{\text{st}}$, 2$^{\text{nd}}$ and 4$^{\text{th}}$ order.

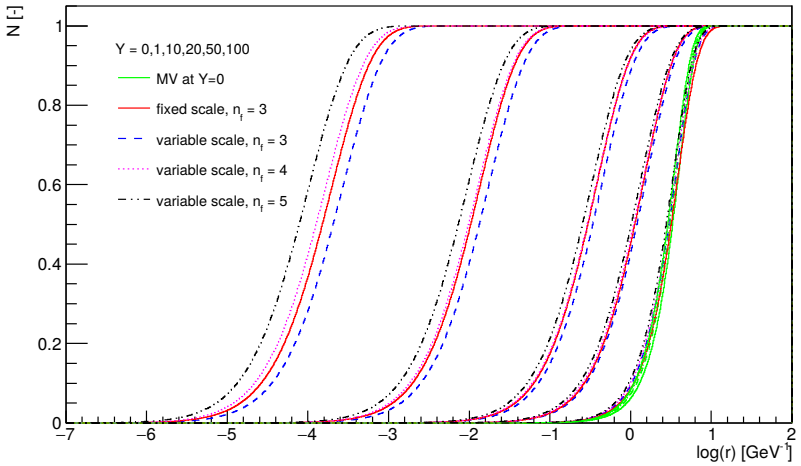

Figure 2: Evolution of the scattering amplitude $N(r, Y)$ of a $q\bar{q}$ dipole with a hadronic target up to rapidity $Y = 100$ for fixed scale with $n_f = 3$, $\Lambda_{fix} = 0.241$ MeV and variable scale for $n_f = 3, 4, 5$, $\Lambda_3 = 0.144$ MeV, $\Lambda_4 = 0.119$ MeV and $\Lambda_5 = 0.087$ MeV.

References

[1] J. Čepila and J. G. Contreras, *Rapidity dependence of saturation in inclusive HERA data with the rcBK equation*, arXiv:1501.06687 [hep-ph].

[2] J. L. Albacete, N. Armesto, J. G. Milhano, P. Quiroga Arias and C. A. Salgado, Eur. Phys. J. C (2011) 71: 1705.

Azimuthally sensitive femtoscopy

Jakub Cimerman *(jakub.cimerman@gmail.com)*

1 Introduction

1.1 Emission function

Emission function is defined as probability, that a particle with 4-momentum p is emitted from spacetime point x. Formally it is a Wigner phase-space density. By integrating emission function through volume of fireball we get momentum spectrum

$$P(p_t, \phi) = \frac{\mathrm{d}^3 N}{p_t \mathrm{d}p_t \mathrm{d}Y \mathrm{d}\phi} = \int S(x,p) \mathrm{d}^4 x. \tag{1}$$

Since this spectrum is azimuthally dependent, we can decompose it into Fourier series, where Fourier coefficients can be expressed as

$$v_n(p_t) = \frac{\int_0^{2\pi} P(p_t, \phi) \cos(n(\phi - \theta_n)) \mathrm{d}\phi}{\int_0^{2\pi} P(p_t, \phi) \mathrm{d}\phi}. \tag{2}$$

1.2 Correlation function

Correlation function is defined as ratio of two-particle spectrum and one-particle spectra. We can write its formula using terms $K = \frac{1}{2}(p_1 + p_2)$ as average 4-momentum and $q = p_1 - p_2$ as momentum difference in form

$$C(q,K) - 1 \approx \frac{|\int \mathrm{d}^4 x S(x,K) \exp(iqx)|^2}{\left(\int \mathrm{d}^4 x S(x,K)\right)^2}. \tag{3}$$

Correlation function can be approximated by Gauss distribution as

$$C(q,K) - 1 \approx \exp\left(-R_o^2 q_o^2 - R_s^2 q_s^2 - R_l^2 q_l^2 - 2R_{os}^2 q_o q_s - 2R_{ol}^2 q_o q_l - 2R_{sl}^2 q_s q_l\right), \tag{4}$$

where R_i are correlation radii[1]. They tell us information about size of homogeneity region of fireball.

1.3 Blast-wave model

Blast-wave model is theoretical model characterized by emission function

$$S(x,p)\mathrm{d}^4 x = \frac{m_t \cosh(\eta - Y)}{(2\pi)^3} \mathrm{d}\eta \mathrm{d}x \mathrm{d}y \frac{\tau \mathrm{d}\tau}{\sqrt{2\pi}\Delta\tau} \exp\left(-\frac{(\tau - \tau_0)^2}{2\Delta\tau^2}\right) \exp\left(-\frac{p^\mu u_\mu}{T}\right) \Theta\left(1 - \overline{r}\right) \tag{5}$$

[1] also called HBT radii

We implemented two kinds of anisotropy into this model: spatial and flow. Spatial anisotropy describes shape of the fireball and is parametrized in Fourier decomposition of fireball radius. Flow anisotropy describes distribution of transverse rapidity.

2 Emission functions of different sources

Consider Gaussian emission function with elliptical anisotropy

$$S(x, y) \propto e^{-ax^2-by^2+2cxy}. \tag{6}$$

Correlation function of this emission function is then

$$C(q) - 1 = e^{-R_1^2(q_o \cos\theta_2 - q_s \sin\theta_2)^2 - R_2^2(q_o \sin\theta_2 + q_s \cos\theta_2)^2}, \tag{7}$$

where R_1 and R_2 are sizes of fireball. In experiment, we sum correlation functions over many events, what can affect the shape of correlation function. To reproduce it within our model, we have to integrate correlation function over different sizes R_1, R_2 and azimuthal angle θ_2. Then we fit resulting function by Lévy distribution $\exp(-|qR|^\alpha)$ to see, how the shape of correlation function changed and how far from Gaussian function it is.

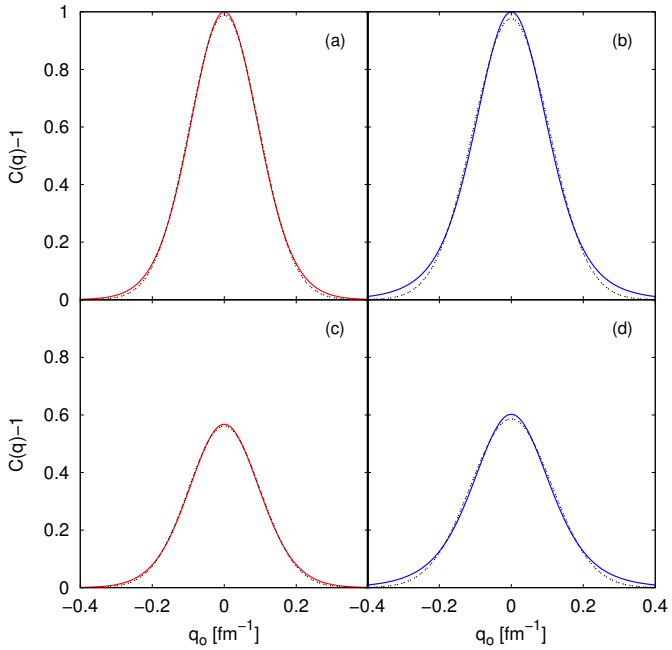

Figure 1: On this plots you can see cuts of resulting correlation function. There is cut with $q_s = 0\,\mathrm{fm}^{-1}$ (upper row) and $q_s = 0.1\,\mathrm{fm}^{-1}$ (lower row). We considerd uniform (left column) and nonuniform (right column) distribution of sizes. Resulting function is represented by color line and black dashed line is Gaussian fit. Lévy coefficient α is (a) 1.8659, (b) 1.7052, (c) 1.8661 and (d) 1.6806.

3 Femtoscopy with similar events

To study femtoscopy on similar events we use simulations of events. The process to simulate events and calculate azimuthal dependence of correlation radii is:

- we generate events with DRAGON[1] and AMPT[2] simulators
- we sort events by its shape with Event Shape Sorting algorithm[3]
- we calculate correlation function with CRAB[4] (CoRrelation After Burner)
- By fitting correlation function we get correlation radii

After sorting events, we split them into 10 classes. We can calculate v_2 and v_3 from azimuthal distribution of particles for each class. We can also obtain azimuthal dependece of correlation radii in each class. Then we can decompose R_o^2 and R_s^2 into Fourier series and calculate series' coefficients. Evolution of all these coefficients across classes shows us, how the average shape is changing.

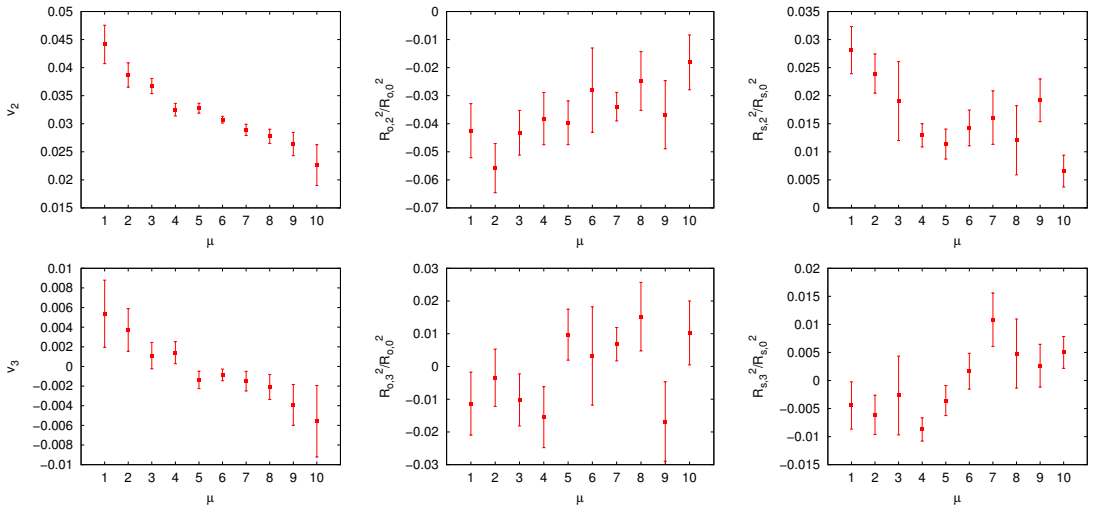

Figure 2: Evolution of fireball shape in classes of sorted events. There are coefficients of Fourier series of particle spectrum (first column), R_o (second column) and R_s (last column). We can see both second (upper row) and third (lower row) order anisotropies.

References

[1] B. Tomášik, Comp. Phys. Comm. 180, 2087 (2005)

[2] Z. Lin et al, Phys. Rev. C 72, 064901 (2005)

[3] R. Kopečná, B. Tomášik, Eur. Phys. J. A 52, 16115 (2016)

[4] S. Pratt, [online] http://www.pa.msu.edu/pratts/freecodes/crab/home.html

Dowm-ramp in LWFA and gas density measurement.

Ekaterina Eremenko*(eremeeka@fjfi.cvut.cz)*

1 Laser acceleration

Accelerated charged particles are widely used in medicine, industry and physical research. Conventional accelerators have a 100 MV/m electric field limit mainly due to the break-down on the walls of the accelerator. To reach requested energies, accelerators in scale of hundred of meters should be built. Laser-based accelerators can sustain significantly higher electric fields (up to 3 TV/m for laser intensity $\sim 10^{18}$ W/cm^2) on the millimeter scale.

Laser pulse propagating through plasma excites plasma waves, which leads to the electric field production. Produced plasma wave phase velocity v_φ is equal to the laser group velocity v_g. When the charge is displaced in the neutral plasma, electric field will be produced, trying to return the charge on its initial place. Laser pulse moving through plasma pushes electrons away from its focus. It is possible due to the ponderomotive force, which depends on the gradient of laser electric field squared. Due to this two opposite forces electrons start to oscillate and it leads to the lack of electrons behind the laser pulse, which creates strong longitudinal electric field. Electron beam placed in this laser wakefield can be accelerated to high energies over small distance.

2 Controlled injection

To get controlled mono-energetic electron beam, particles should be somehow injected to the plasma waves. Various techniques can be used, for example self-injection, colliding pulse injection, ionization injection and down-ramp injection.

The easiest to implement is the self-injection technique, which uses the plasma wave breaking to inject electrons. In most cases beam obtained by this technique is not stable or mono-energetic, so it cannot be used in further applications.

The down-ramp injection uses the downward density ramp with a density gradient scale length L_{grad} greater than the plasma wavelength λ_p to control the injection due to the wave breaking. Decrease in plasma phase velocity in the density down-ramp causes lowering of the threshold of background electrons trapping and wakefield wave breaking. To achieve density down-ramp part of the supersonic gas jet can be covered to produce a shock front or other smaller nozzle can be inserted into to the jet.

3 Gas density measurement

For controlled beam production gas profile above the supersonic nozzle should be measured. Interferometry and deflectometry techniques can be used for this purpose. These two techniques are optical methods that use properties of light.

Mach-Zehnder interferometer splits the laser ray with beam splitter, one beam propagates through vacuum and other through the chamber with the supersonic nozzle, where the shift in the phase of the ray appears according to the density gradient. Second beam splitter merge the rays together and due to the phenomenon of interference displays the density profile of the nozzle, which can be than detected with the CCD camera.

The simplest deflectometry technique is shadowgraphy, that is using the fact that any air disturbance can refract the light rays and in the result the density gradient can be seen in shadow of the nozzle.

Moire deflectometry is similar to the shadowgraphy, but uses two separated in space grids, placed between the object and the mat screen. The superposition of images from the grids is viewed on the screen as, so called, moire pattern.

Each technique has a different advantages, for example interferometer can measure higher densities, shadowgraphy is easy to implement and moire deflectometry has a higher sensitivity. To get better density profile few techniques can be performed simultaneously.

References

[1] K. Swanson, H. Tsai, Phys. Rev. Accel. Beams. 20, 5, 1–6 (2017)

[2] V. Malka, J. Faure, Eur. Part. Accel. Conf. EPAC, 26–30 (2006)

[3] I. Glatt, O. Kafri, Opt. Lasers Eng., 8, December 1987, 277–320 (1988)

Coherent photoproduction of ψ(2S) vector mesons in Pb–Pb UPC

Zuzana Gajdošová*(gajdozuz@fjfi.cvut.cz)*

One of the open questions in QCD today is the cause of the shadowing phenomenon in nuclei. To understand this phenomenon it is necessary to study gluon distributions in nuclei at small x. There are several models trying to describe such phenomenon in QCD which have to be experimentally scrutinised and confirmed. One of the suitable processes to investigate gluon distributions in nuclei is the coherent photoproduction of a vector meson. The measurement of its cross section can serve as a verification of one or more theoretical predictions of this QCD phenomenon.

We prepared tools for the calculation of the cross section of the coherent photoproduction of the vector meson ψ(2S) in mid-rapidity, see eq. (1), such as determination of the yield of ψ(2S) $N^{\rm coh}_{\psi(\rm 2S)}$, the calculation of luminosity $\mathcal{L}_{int}$, the determination of the product of the acceptance and efficiency $(\rm Acc \times \epsilon)_{\psi(2S)}$ and estimation of some related systematic uncertainties. The studies were performed with data from Pb–Pb collisions at a centre-of-mass energy $\sqrt{s_{\rm NN}} = 5.02$ TeV collected during the Run 2 data-taking period at the LHC with the ALICE detector at mid-rapidity.

$$\frac{{\rm d}\sigma^{\rm coh}_{\psi(\rm 2S)}}{{\rm d}y} = \frac{N^{\rm coh}_{\psi(\rm 2S)}}{(\rm Acc \times \epsilon)_{\psi(\rm 2S)} BR(\psi(\rm 2S))\mathcal{L}_{\rm int}\Delta \rm y} \tag{1}$$

The coherent yield of the ψ(2S) was studied in 4 different decay channels: the direct one, $\psi(\rm 2S) \rightarrow l^-l^+$, where l stands for lepton and it can be either electron or muon. The other two studies were the decay of ψ(2S) into 4 products, i.e. $\psi(\rm 2S) \rightarrow J/\psi\pi^-\pi^+$, where $J/\psi \rightarrow l^-l^+$. We reconstructed the coherent yield of the ψ(2S) from simulations of the collision of Pb–Pb which were folded with the simulated ALICE detector. Then we analysed the simulation of the generated yield of ψ(2S) in a given rapidity range, i.e. the simulation of a collision which was not influenced by the imperfection of the detector. Dividing these yields, reconstructed over generated, we studied the acceptance and efficiency product, i.e. how many event candidates we lost due to the imperfection of the detector. We also calculated the integrated luminosity, which was the last step necessary to obtain $\frac{{\rm d}\sigma^{\rm coh}_{\psi(\rm 2S)}}{{\rm d}y}$. The corresponding branching ratio of the ψ(2S) decay channel can be seen in Table 1.

The measurement of the cross section at this rapidity region and with almost 2 times higher energies than in Run 1 will provide an important contribution to the search for the origin of the shadowing.

Decay channel	Branching ratio
$\psi(2S) \to J/\psi + \pi^-\pi^+$	$34.00\% \pm 0.40\%$
$J/\psi \to \mu^- + \mu^+$	$5.93\% \pm 0.06\%$
$J/\psi \to e^- + e^+$	$5.94\% \pm 0.06\%$

Table 1: Branching ratio of different $\psi(2S)$ decay channels [1].

References

[1] K. A. Olive et al. Review of Particle Physics. *Chin. Phys.*, C38:090001, 2014

Laser pulses synchronization for perpendicular electron bunch injection into the accelerating phase of laser-driven plasma wave

Pavel Gajdoš*(gajdopa1@fjfi.cvut.cz)*

1 Introduction

Laser-driven plasma waves are able to sustain large acceleration gradients. These gradients can be used for electron acceleration. To obtain a high-quality electron bunch an injection mechanism is needed. There are several mechanisms of electron injection. The simpliest method is a self-injection [1], however, it is very unstable and electron bunches have large energy spreads. Therefore, more stable methods such as ionization injection [2] and downramp density transition [1] have been developed and done experimentally.

This paper suggests an optical technique for another injection method, which uses perpendicularly crosing laser pulses, based on a numerical simulation [3. In Sec. 2 the mechanism of injection and results from numerical simulation are shown. In Sec. 3 the concept of an optical system is described.

2 Perpendicularly crossing pulses

The main idea of this injection is the use of two laser pulses with different intensity. The strong drive pulse creates a plasma wave and the weak pulse injects electron into a acceleration phase of the wave. For numerical simulation [3] following parameters were used: plasma density: $n_e = 5 \times 10^{18}$ cm^{-3}, drive pulse wavelength: $\lambda = 0.8\mu$m, pulse length (FWHM): $\tau = 25$ fs, and drive pulse intensity: $I_{DP} = 3.42 \times 10^{19}$ W/cm^2. The weak injection pulse differs only with intensity. Polarization of both pulses is linear with mutually perpendicular polarization vector. Crossing of these two pulses is in the same focal spot. The configuration is so-called Orthogonally Crossing Pulses with Perpendicular Polarization (OC3P).

As shown in Fig. 1 this injection is formed with three different mechanisms depending on an initital position of trapped electrons. The large number of electrons ($\approx 70\%$) are trapped by the *crossing beatwave injection* (represented by blue color in Fig. 1). Firstly, they are expelled out of the high intensity in the crossing region and then accelerated by the field of the plasma wave. A smaller number of electrons ($\approx 20\%$) are accelerated by the *injection by the laser field preacceleration* (red in Fig. 1). These electrons are firstly

dephased by the collision of pulses and then trapped and accelerated by the drive pulse. The last small fraction of electrons (black in Fig. 1) are accelerated due to the mechanism similar to self-injection. The second pulse is not needed to trap these electrons.

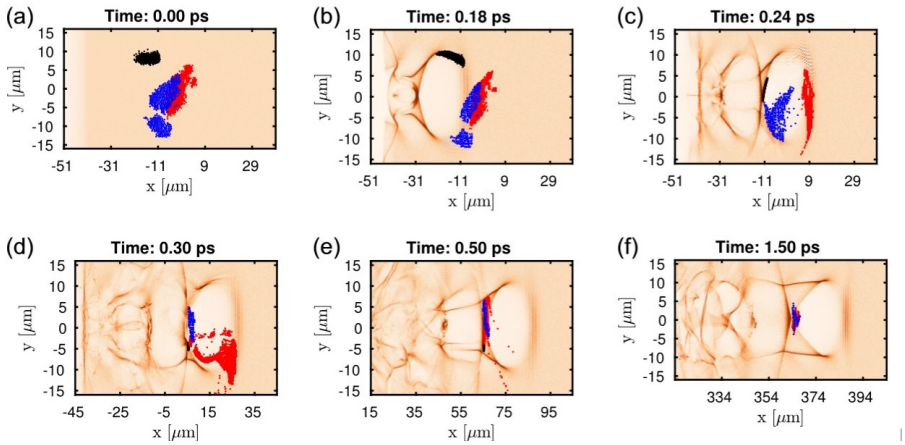

Figure 1: Time sequence of electron position, [3]

The important result that comes from the simulation is the intesity of the injection pulse. Fig. 2 shows comparision of energy spectra of accelerated electrons for two different intensities of injection pulse and drive pulse only. The case with the lower intensitiy injection pulse ($I_{IP} = 0.01 I_{DP}$) is a better choice because of smaller energy spread and peak energy slightly moved to higher energies.

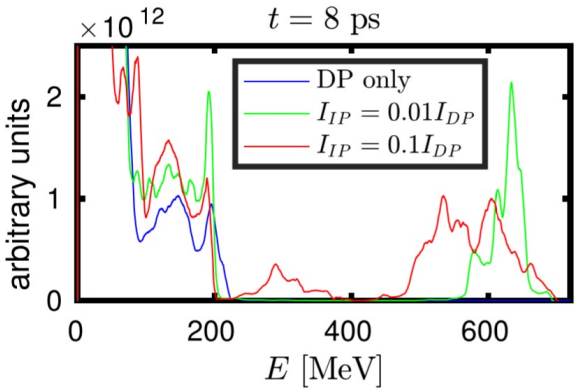

Figure 2: Energy spectra of accelerated electrons for two different intensities of injection pulse and drive pulse only, [3]

3 Optical system

Because of need of perendicularly crossing pulses our optical system is based on Mach-Zehneder interferometer with added off-axis paraboloids (**OAP**) with focal spot lengths $F_1 = 272$ mm and $F_2 = 163$ mm and off-axis angles of 30° for focusation of each laser beam. The scheme of our system is in Fig. 3. A laser beam is firstly divided by a beam

splitter (**BS**) and both beams are focused onto another beam splitter on the same focal spot using mirrors (**M**) and **OAP**. This system has been tested using red He-Ne laser to show interference. After that, the delay line consisting of four mirrors was added for adjusting the length of trajectory of one beam since the use of fs lasers requires exactly the same length of trajectories of both beams, otherwise interference does not occur. For practical use the second beam splitter will be replaced with the gas jet.

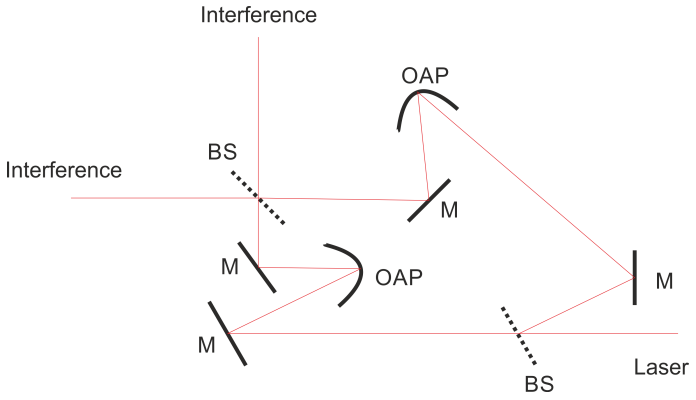

Figure 3: Scheme of the optical system. Laser beam is divided by beam splitter (**BS**) and using mirrors (**M**) and off-axis paraboloids **OAP** focused onto another beam splitter

4 Conclusion

An overview of the perpendicular crossing pulses mechanism was shown in Sec. 2. The highest quality electron beam is produced when the intensity of the injection pulse is 1 % of the intensity of the drive pulse. The suggested optical system was described in Sec. 3. Intereference occured when He-Ne laser was used. After optimalization of off-axis paraboloids and ensuring of spatial overlay of both focal spots this system will be tested using Ti-Sapphire laser system in PALS[1].

References

[1] E. Esarey, C. B. Schroeder, and W. P. Leemans, Physics of laser-driven plasma-based electron accelerators, Rev. Mod. Phys. 81 (2009) 122

[2] Chen et al., Electron injection and trapping in a laser wakefield by field ionization to high-charge states of gases, Journal of Applied Physics 99, 056109 (2006)

[3] Horný et al., Short electron bunches generated by perpendicularly crossing laser pulses, Phys. Plasmas 24 (2017) 103125

[4] D. J. Corvan et al., Femtosecond-scale synchronization of ultra-intense focused laser beams, arXiv:1407.4243v1

[1]PALS - Prague Asterix Laser System

Correlation femtoscopy at the STAR experiment

Lukas Holub*(lukas93@rcf.rhic.bnl.gov)*

The one-dimensional uncorrected correlation functions for Bose-Einstein correlation, that means that we did not include Coulomb interaction between particlesno, are fitted by

$$\begin{aligned} C_{Gauss}(\vec{q},\vec{k}) &= 1+\lambda(\vec{k})e^{-(q_{inv}R_{inv}(\vec{k}))^2} \\ C_{Levy}(\vec{q},\vec{k}) &= 1+\lambda(\vec{k})e^{-|q_{inv}R_L(\vec{k})|^\alpha}. \end{aligned} \tag{1}$$

The first equation is well known Gaussian distribution, here q_{inv} is the Lorentz invariant momentum defined in (Eq. 1), R_{inv} is the Lorentz invariant radius and λ is the chaoticity parameter. The second equation is the Levy distribution, here q_{inv}, R_L and λ have the same meaning as in the case of the Gaussian distribution but α is the Levy index called also index of stability, which can be equal to the values $0 < \alpha \leq 2$. There are two specific case, at $\alpha = 2$; the Gaussian parametrization corresponded to the normal (Gaussian) distribution function

$$S_{\vec{k}}(\vec{x}) = \frac{1}{\sqrt{2\pi R_G^2}} e^{-\frac{(x-x_0)^2}{2R_G^2}}, \tag{2}$$

where the Gaussian scale parameter is $R_G^2 = \langle x^2\rangle - x_0^2$, the standart deviation. Another specific case of the Levy distribution is at $\alpha = 1$ which is called exponential parametrization and it corresponds to the Cauche (Lorentzian) distribution function

$$S_{\vec{k}}(\vec{x}) = \frac{R_c}{\pi(R_c^2+(x-x_0)^2)}, \tag{3}$$

with scale parameter R_c. For more details about Levy distribution see [**?**].

Figures (Fig.1) show examples of one-dimensional correlation functions for different reference multiplicity ranges: 0-60, 0-15, 15-30, 30-45, 45-60, respectively. In each multiplicity range, k_T is divided into five bins as was mentioned previous. Due to poor statistic we have not considered and described correlation functions for multiplicity bins 45-60.

One can see that fits do not include an area where the Coulomb interaction has a significant influence, (small q_{inv}). In order to fit this data with the Coulomb interaction one has to use different models unlike (Eq.1) but this is not the main idea of this work. As can be seen from comparison of the fits, almost in all cases the Levy fits better describe data than the Gaussian fits which means that the source is of non-Gaussian shape. In the figures we can also see χ^2 however, in our cases this test is not very useful because as can be seen fits do not do not describe data properly.

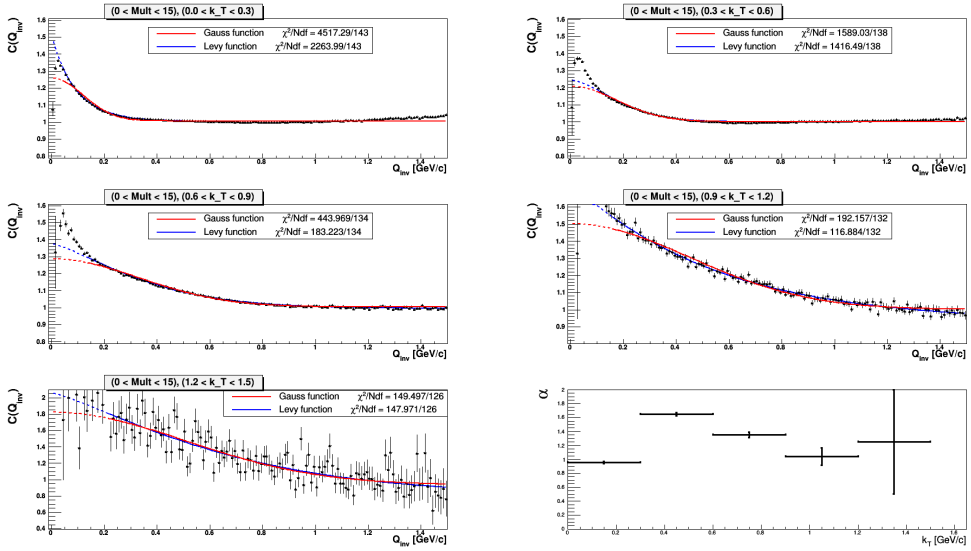

Figure 1: One-dimensional correlation function for positive pions for multiplicity 0-60 and five k_T bins. The lines represent fits to the data by using (Eq.1). On the left side down is plotted dependence of levy parameter (α) as a function of k_T.

Results from fits of correlation functions for different multiplicities and k_T bins are presented in (Fiq.2 and Fig.3). Here the λ parameter and source radius R_{inv} and R_L are shown as a function of the multiplicity and pair transverse momentum k_T.

As we mentioned, the source radii R decrease with the pair tranverse momentum k_T for the Levy distribution as well as for the Gaussian distribution. This behaviour qualitatively agrees with the effect expected from a system undergoing a transverse expansion where pairs with the larger transverse momentum are emitted from a smaller homogeneity region than the pairs with the smaller k_T, as it was discussed in Chapter 4. A dependence of the radii R_{inv} and R_L on the multiplicity is already not such clear. One would expect that with higher multiplicity the radii of the homogeneity region increase however it is hard to confirm this fact from the (Fig.3). As we can see, for the Gauss radii this dependence can be observed in a range of errors but for the Levy radii such a behaviour is not observed. For this observation a more precise analysis must be done.

The behaviour of the λ parameter is not monotonic. In the case of Levy distribution, for small multiplicities this parameter decreases for lower k_T bins and then increases while for bigger multiplicities it is almost constant for lower k_T bins and then it increases. For Gaussian distribution this parameter decreases very weakly, it is almost constant for lower k_T bins but then it increases too.

References

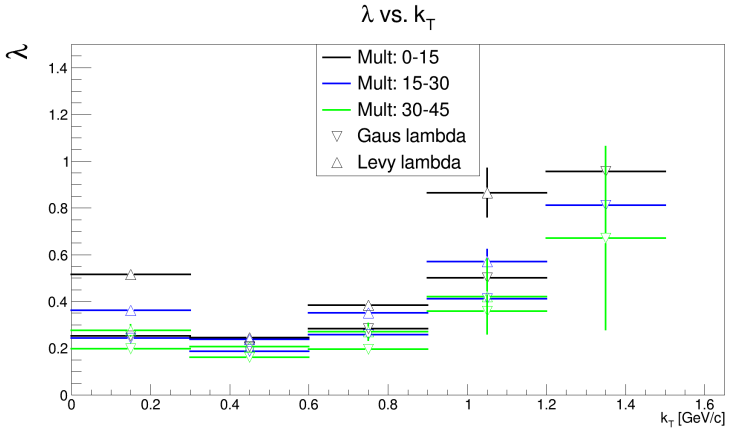

Figure 2: Fit results: λ as a function of k_T and multiplicity for Levy and Gauss distribution.

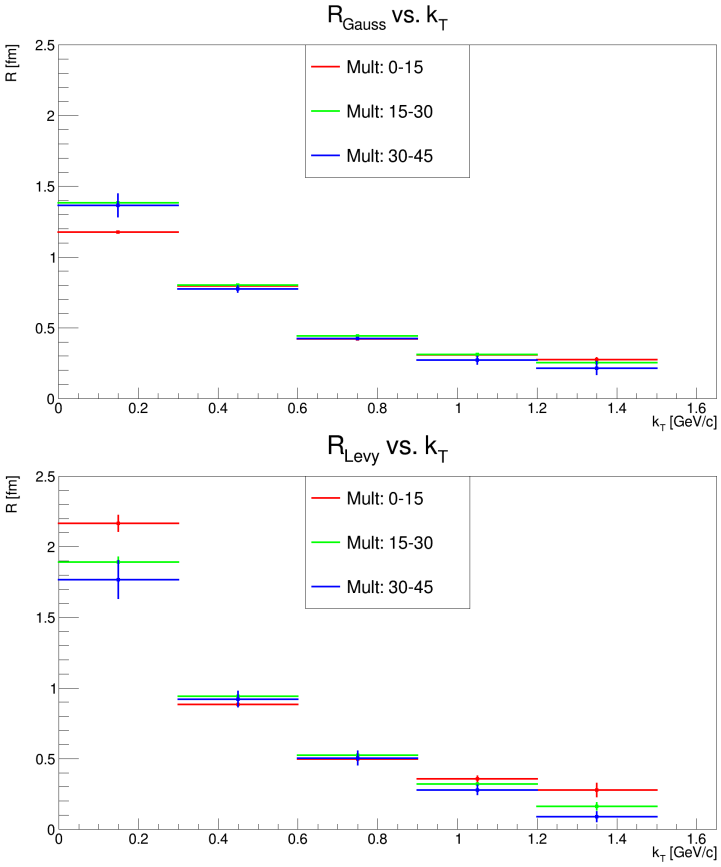

Figure 3: Fit results: R_{inv} and R_L as a function of k_T and multiplicity. Top panel is for Gaussian distribution. Bottom panel is for Levy distribution.

Space Environment

Anežka Kabátová*(anezka.kabatova@gmail.com)*

1 Introduction

In order to design a detector for the space environment we need to learn about processes happening in a near-Earth space. Shortly after 1958, when the satellite era began, James Van Allen discovered belts of high-energy particles rich with protons and electrons. However, these particles are not the only ones that can possibly encounter manned as well as unmanned missions on orbit. The most important source and modulator of a space radiation is the Sun. Predictions and detection of the Sun activity should stand in the center of our attention and research to provide safety for astronauts and expensive electronics sent in space. The last key contributors on the space environment discussed in this paper are galactic cosmic rays (GCR) which are strongly dependent on the phase of the Sun activity [1].

2 Sun activity

The Sun activity is not constant in time. It pursues a 11-year-long asymmetric cycle of 7 years of solar maximum and 4 years of solar minimum. At the end of this cycle, the polarity of a solar magnetic field changes and another cycle follows. The phase of the solar activity cycle has major impact on it's own particle production, but also on fluxes of GCR and particles trapped in Van Allen belts. During the declining phase, which is slightly longer than the increasing one, large proton events occur with high frequency and fluxes of trapped electrons reach their maxims. In the solar activity minimum, GCR are on the maximum. This is a demonstration of the importance of a solar activity monitoring. Rough prediction can be made when we look at the development of the number of sunspots or values of $F_{10.7}$ radio flux (Fig. 1) [1].

3 Galactic cosmic rays

Galactic cosmic rays (GCR) are high energy particles with origin outside the Solar System. Energies which these particles can reach are enormous (as high as 10^{11} GeV). However, the mechanism of their acceleration is not clear yet. GCR consist of all elements in Periodic Table up to the uranium with steep drop-off after the iron [1]. GCR are due to the greatest part of Single Event Effects (SEE) in electronic devices [2]. A way of quantification of SEE is the linear energy transfer (LET), which is defined as the energy

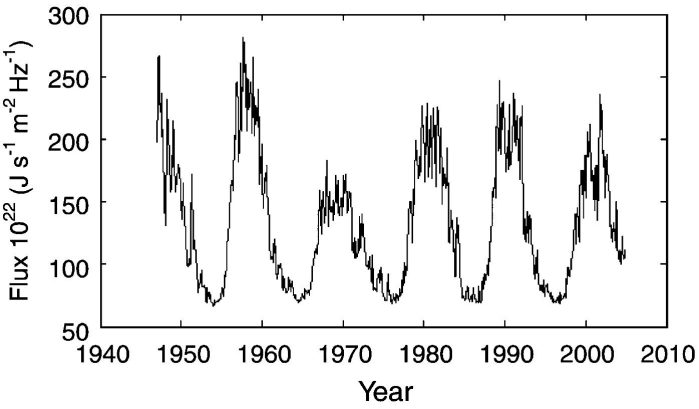

Figure 1: Radiation flux with $\lambda = 10.7$ cm time development, [Boudarie, 2008]

deposited by particle per unit path length in the sensitive volume [1]. LET stands in the center of focus during a development of a semiconductor detector.

4 Earth radiation belts

The Earth's magnetosphere protects our planet from external influences. Most of the particles encountering this cavity is deflected away. However, at the level of poles, the shape of the magnetosphere (Fig. 2) allows cosmic particles to reach the Earth's upper atmosphere. There, due to the magnetic field, particles can be trapped in radiation belts, which we call Van Allen belts. The lower limit of Van Allen belts is the atmosphere, but the upper limit is indistinct. Approximately, their occurrence fluctuates between 400 and 50 000 km. Van Allen belts are rich with protons and electrons with energies at most hundreds of MeV [1].

The Earth's magnetic field is not symmetric - it can be approximated by a tilted dipole. This irregularity results in formation of a zone where the magnetic field is weaker. Therefore, radiation belts are lowered in this area, which is called South Atlantic Anomaly. In Fig. 3 can be seen that missions on Lower Orbit are endangered by trapped particles at the level of poles and the South Atlantic Anomaly [1].

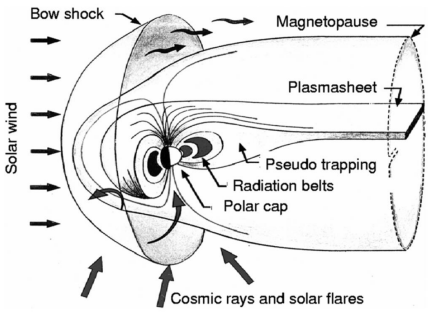

Figure 2: Scheme of Earth's magnetosphere, [Boudarie, 2008]

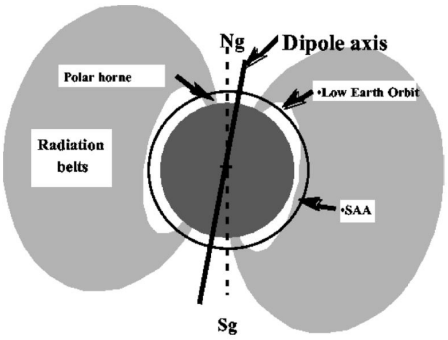

Figure 3: Scheme of exposure to trapped particles on Low Orbit, [Boudarie, 2008]

5 Summary

Missions on orbit are exposed to an extremely variable environment of high-energy particles with diverse origin. The main contributor to the variation of particle fluxes is the Sun, whose activity follows a cycle of 11 years. During this cycle, fluxes of it's own particles as well as GCR and radiation belts change.

Electronic devices in the space suffer from cumulative effects of the radiation, but also from Single Event Effects that can result in destruction of the device. Manned missions need even better protection to preserve it's crew from a cancer development and other effects of exposure to radiation doses.

For this reason, we need reliable predictions and universal detectors that can resist in these extreme conditions.

References

[1] S. Boudarie, M. Xapsos The Near-Earth Space Radiation Environment *IEEE Transactions on Nuclear Science*, 55(4):1810-1831, 2008.

[2] *Space Flight Environment International Engineering Newsletter*, 4(4) 2008.

Study of the QGP medium with heavy quarkonia

Martin Klíštinec*(klistmar@fjficvut.cz)*

1 Quark-gloun plasma

Quark-Gluon plasma is an extreme form of matter, where quarks do not create a bound state.

1.1 Phase diagram

Baryon chemical potential μ_B measures the imbalance between matter and antimatter, and zero indicates perfect balance. Science believe that before the critical point the phase transition is not continuous. After the critical point the transition is continuous.

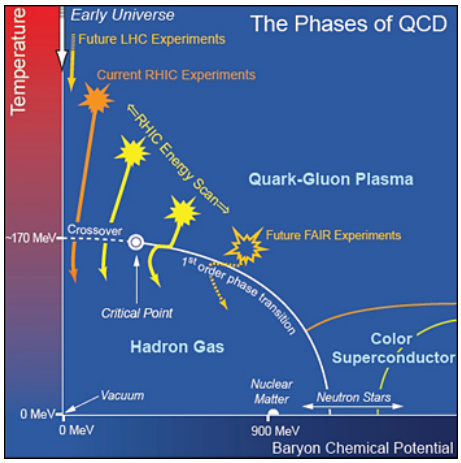

Figure 1: Phase diagram of matter.

1.2 Time evolution of QGP

When two particles colide in a accelerator two posibilities may happen, creating QGP and not creating QGP. With QPG there are several phases: pre-equlibrium, thermal equlibrium (we can use laws of electrodynamic to describe the QGP), mixed, hadron gas. Also between the mixed phase and hadron gas there is a chemical freeze-out and after hadron gas phase, there is a freeze-out. Chemical freeze-out is a point where particles stop intereact inelasically and freeze-out is a point where particles stop intereact elastically. Without a QGP there is only hadron gas phase followed by freeze-out.

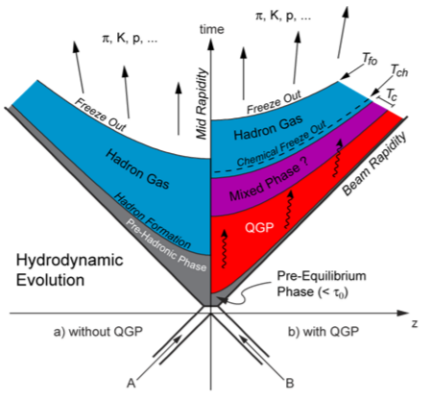

Figure 2: Time evolution of QGP.

1.3 Heavy quarkonia

Heavy quarkonia are bound state of quark and anti-quark($b\bar{b}$, $c\bar{c}$). The reason why we study heavy quarkonia is that, they are created in the beginning of the collision and they will survive the whole evolution of the medium.

2 Suppression, enhancement of production of heavy quarkonia

2.1 Nuclear modification factor

By using data from p+p collisions (without QGP) we can compute how many Υ particles from Au+Au collisions (with QGP) we can expect and the ratio of real data and the computed is called nuclear modification factor R_{AA}. If $R_{AA} < 1$ then there is a suppression and if $R_{AA} > 1$ then there is an enhancement.

2.2 Melting and recombination

The effects of hot nucelear matter are melting and recombination. They are based on *Debye screening*. It tells us that range of the strong interaction is decreasing as $\approx \frac{1}{\sqrt{T}}$, where T is the temparature of the medium. After certain temparature the quarkonia no longer can create a bound state and quarks can move freely. This effect can cause suppresion and enhancement.

2.3 Nuclear (anti)shadowing

These effects come from the gluon fusion and recombination between different nucleons in a nucleus, which change the distributions of gluon and quarks but not their total momentum.

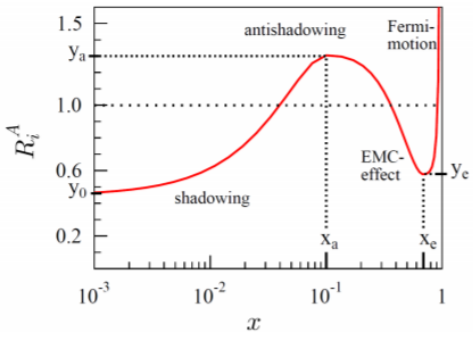

Figure 3: Time evolution of QGP.

2.4 Other effects

1. Cronin efect
2. Interaction with comovers
3. Feed-down efect

References

[1] Kesich, Antony Robert, Upsilon production and supprresion as measured by STAR in p + p, d + Au and Au + Au Collision, University of California.

[2] Fodorová, Jana, Production of J/ψ meson in central U+U collisions at the STAR experiment, Czech technical university.

Dose distributions of different particles in a water phantom

Tadeáš Kmenta*(kmenttad@fjfi.cvut.cz)*

1 Introduction

This proceeding is a summary of Dose Distribution paper [1]. It is highly recommended to the reader to take a look at the paper as this proceeding does not contain figures nor tables or in depth explanation.

1.1 FLUKA

FLUKA is a Monte Carlo software that simulates radiation matter interaction. FLUKA allows to simulate interaction of more then 60 different particles in a wide energy range. In addition to that, FLUKA can handle very complex geometries, does not require any programming skills for most applications and offers FLAIR user interface.

1.2 Measurement procedure

The results are obtained by running programmable input files written in FLUKA code. Every simulation was run with 1 million primary particles for 5 cycles. Carbon ions were run with custom executable which was compiled using FLUKA compile module linking *dpmjet (\$FLUPRO/flutils/ldpmqmd)*. The obtained data from the simulation can be put into readible figures as are those in [1].

1.3 Dose distribution

Dose deposited is a physical dose quantity representing the mean energy imparted to matter per unit mass by ionizing radiation. The standard unit of deposited dose is J/Kg, and its special name is gray (Gy). FLUKA scores Dose deposited in GeV/g. To obtain scored dose in Gy, multiply GeV/g by $1.602176462 \times 10^{-7}$.

Dose distribution is represented by an image showing the dose deposited at a given depth and radius. In this simulation a block instead of a cone was used, therefore radius is represented by X, Y respectively.

2 Results

2.1 Photons

Dose distribution for 10 MeV and 25 MeV Photon beam was scored. These energies were chosen to score as they are one of those currently being used in radiotherapy.

The higher the energy the bigger the dose deposited but also more surrounding material is affected which is not desired in radiotherapy. The beam particles (only the particles that were shot) are basically irrelevant in the total dose deposited but create many secondary particles primarily via Compton scattering.

Total dose deposited only consists by the dose deposited by photons, electrons and positrons. According to FLUKA scoring for other particles, no other particle is responsible for any other dose. Most of the dose is deposited by electrons followed by positrons with photons having some effect as well. This fact is important as it may be possible to better focus the dose deposited via magnets and may allow to use higher photon energies while keeping the most of the total deposited dose pretty narrowed and thus sparing the healthy tissue.

2.2 Electrons

Dose distribution for Electrons was scored for 10 MeV and 25 MeV primary particles as well as for very high energy electrons of 150 MeV, 200 MeV and 250 MeV. These energies were chosen as they reflect the ones currently used in radiotherapy and in case of very high energy electrons cover and demonstrate currently studied energy spectrum for future radiotherapy application.

Total dose deposited only consists by dose deposited by photons, electrons and positrons. According to FLUKA scoring for other particles, no other particle is responsible for any other dose.

Majority of the dose is deposited by the beam particle itself, however the beam particle is also causing many secondary electrons, positrons and photons that also contribute to the total dose. The higher the energy the bigger role these secondaries play especially positrons. There is also a significant difference in the shape of dose deposited comparing low energy and high energy electrons.

2.3 Protons

Dose distribution for 100 MeV and 200 MeV proton beam was scored. These energies were chosen to score to clearly demonstrate the differences between energies while being currently used in radiotherapy.

The higher the energy of the beam the further the Bragg peak occurs and the bigger total dose deposited. Maximum dose is deposited in the distance of the Bragg peak. The vast majority of the dose is caused by the beam particle itself and secondary particles are at least an order of magnitude lower in case of electromagnetic dose. The total dose deposited consists also of the dose deposited by other particles such as Helium ions or deuterons althougt this dose was not scored. These particles are being created in non-elastic nuclear reaction between proton beam particles and atomic nuclei of water phantom.

2.4 Carbon ions

In the case of carbon ions, 100 MeV/u and 200 MeV/u carbon beams were scored to have direct comparison with the case of proton beams.

The total dose deposited of carbon ions is way bigger then by other particles and is concentrated in a smaller area around the beam. In addition, most of the dose is deposited in the depth of Bragg peak which is taking place earlier then in proton examples. As was in the case of protons, primary beam particles are the most responsible for the total dose deposited while still causing many secondary particles to occur and contribute to the total dose deposited. The total dose deposited consists also of dose deposited by Helium ions, deuterons and other heavy ions particles although they were not scored.

References

[1] Dose distributions of different particles in a water phantom, Tadeáš Kmenta, 2018 `http://people.fjfi.cvut.cz/kmenttad/dosedistrib.pdf`, Accessed: 2017-02-06

Charmed Mesons Production in Heavy Ion Collisions

Robert Licenik*(licenik.robert@gmail.com)*

This paper summarizes the physics of charmed mesons in heavy ion collisions. Charmed mesons are mesons that contain a c quark (or antiquark) and serve as an excellent probe in the strongly interacting medium created during heavy ion collisions. This medium is called the quark-gluon plasma (QGP) and it is an object of great interest since it is generally thought that the early Universe (about 1 microsecond after the big bang) went through a QGP phase. The charmed mesons, such as the neutral D^0, the charged $D^{\pm}$ and the strange $D_s^{\pm}$, are created during the earliest stages of the collision and therefore experience the entire evolution of the system. As the heavy quark moves through the medium, which contains free color charges, it interacts with this medium and loses energy via elastic collisions and gluon radiation. The main observable for this process is the modification of the charmed meson yield in nucleus-nucleus collisions compared to proton-proton collisions, where no medium is expected to be created. This modification is characterized by the nuclear modification factor $R_{AA} = \frac{\frac{\mathrm{d}^2 N_{AA}}{\mathrm{d}p_T \mathrm{d}y}}{\langle N_{coll} \rangle \times \frac{\mathrm{d}^2 N_{pp}}{\mathrm{d}p_T \mathrm{d}y}}$, which is the ratio of the invariant yield in A-A collisions and the invariant yield in p-p collisions scaled by the mean number of binary collisions (since we can treat the A-A collision as a large number of nucleon-nucleon collisions). Recent results indicate strong suppression of the charmed meson production in central A-A collisions compared to the p-p collisions (see Fig. 1), especially at higher values of the transverse momentum.

Since the charmed mesons are very short-lived ($c\tau = 312$ μm for $D^{\pm}$ [1]), a detector with supreme tracking capabilities is needed to allow for a precise reconstruction of the secondary vertices which result from the D meson decays to daughter particles (usually kaons and pions). The Heavy Flavor Tracker, capable of spatial resolution of ~ 20 μm, was a part of the STAR experiment between 2014 and 2016 and enabled the analysis of the $D^{\pm}$ meson production for the first time at STAR. After applying several selection criteria to reconstruct $K\pi\pi$ triplets that could be a result of a $D^{\pm}$ meson decay, these triplets were then separated by their charges into two categories: the wrong-sign combinations were treated as a background and the correct-sign combinations were considered for further analysis. Afterwards, additional (mainly topological) selection criteria were applied, to extract those correct-sign triplets that originate from a $D^{\pm}$ meson decay and - after background subtraction - to obtain a $D^{\pm}$ signal. The plans for further analysis include the calculation of the systematic errors, the improvement of signal significance via the use of machine learning methods and to calculate the nuclear modification factor for the 2014 Au-Au collisions at $\sqrt{s_{NN}} = 200$ GeV detected by the STAR experiment.

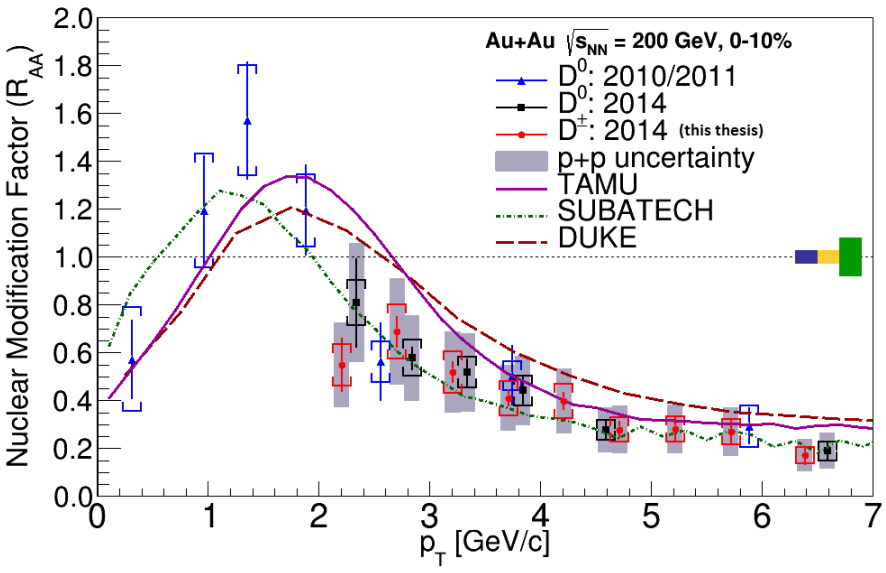

Figure 1: Preliminary results of the $D^{\pm}$ R_{AuAu} in 2014 Au-Au collisions at $\sqrt{s_{NN}}$ = 200 GeV for the 10 % most central collisions as measured by the STAR collaboration. Published results from D^0 measurements are shown as well as several theoretical models. Taken from Ref. [2].

References

[1] C. Patrignani et al. (Particle Data Group), Chin. Phys. C, 40, 100001 (2016) and 2017 update

[2] J. Kvapil, "Charged charm mesons in Au+Au collisions", Master's Thesis, Czech Technical University in Prague, 2016

$D^{\pm}$ measurement in Heavy-Ion Collisions at $\sqrt{s_{NN}} = 200$ GeV at the STAR experiment

Zuzana Moravcová *(zuzana.moravcova@fjfi.cvut.cz)*

Measurements of open heavy flavour mesons can be used to study the properties of the so-called quark-gluon plasma produced in heavy-ion (A+A) collisions, which is a state of hot and dense nuclear matter where quarks and gluons are liberated from hadrons. One of the possible ways to prove the existence of quark-gluon plasma is using the nuclear modification factor. That quantity is the ratio of the yield of a particle in A+A to than in p+p collisions, scaled by the number of binary collisions. In Figure 1, one can observe the suppresion of open charm D^0 and $D^{\pm}$ mesons in transverse momentum p_T range from 2 to 7 GeV/c.

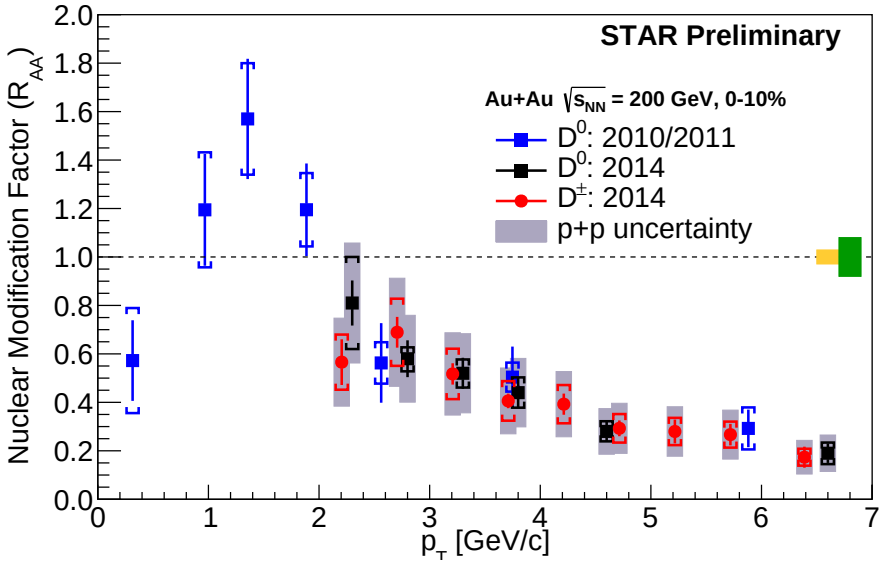

Figure 1: Nuclear modification factor of charmed D^0 and $D^{\pm}$ mesons from the STAR experiment at $\sqrt{s_{NN}} = 200$ GeV. Taken from [1].

Mentioned mesons are not measured directly as they decay very quickly, therefore only their decay products will make a signal in the detector. Since we focus on hadron decay channels in the measurement, in low p_T region we have high combinatorial background. To extract the signal from the background, it is convenient to use machine learning methods.

To analyze data in particle physics, those methods are implemented in package TMVA (Toolkit for Multivariate Data Analysis) [2] within the framework ROOT. We will focus on supervised machine learning, where during the training phase we know both input and output, and on classification algorithms, which divide the data into disjoint sets. In our case, data is subsequently either signal-like or background-like.

Event classification starts with setting of discriminating variables. In case of $D^{\pm}$ mesons, chosen variables are p_T of daughter particles, distances of closest approach, etc. Let us say that we have n variables, which create an n-dimensional space. When $n = 2$, it is easy to visualize the two-dimensional space and choose whether we will use rectangular cuts, linear or non-linear boundary. With rising dimension, the task becomes more complicated. In general, we want to find the function $y(\vec{x})$: $\mathbb{R}^n \to \mathbb{R}$, where for background $y(B) \to 0$ and for signal $y(S) \to 1$. During the training phase the cut value is obtained, everything above the cut value ($y(\vec{x}) > C$) is considered to be a signal (or more precisely, signal-like).

The most elementary and most common method is the rectangular cut optimisation, where for every variable we have an independent cut value (or interval). Then one hypercube from $\mathbb{R}^n$ is considered to be signal-like. In TMVA one can choose different methods to find the right set of cut values, however the genetic algorithms seem to have the best results. [2] This method suffers from the curse of dimensionality – the amount of time needed for training grows exponentially with the number of dimensions. Therefore it is necessary to choose only variables that are proven to have high potential to divide the signal and the background.

If one does not want to limite oneself to only one hypercube, the usage of decision trees is possible. At the begining, the data is stored in the root node, then in every step the data is divided into disjoint subsets based on one variable only. In the following step, either different variable can be used or the same with different borders. Since this method is unstable and can be overfitted easily, we usually use boosting algorithm to improve these imperfections.

Another methods that are widely used are projective likelihood estimator and artifical neural networks. The former is based on Bayesian probability and fails if input variables are non-lineary correlated. The latter is made from interconnected group of nodes called neurons. Three different implementations can be found inside TMVA, from which the multi-layer perceptrons method is the most universal one.

As mentioned above, the multivariate methods using machine learning are used when there is a high combinatorial background in the analysis. In the STAR experiment, the Λ_c particle cannot be found without the TMVA package. Also, the significance of D^0 production was significantly higher – it has risen from 13 (Run10+11) to 51 (Run14) to 1 bilion events[1] [3].

Finally, in my analysis, I will use the TMVA package and find the optimised rectangular cuts for $D^{\pm}$ analysis via the hadron channel. Afterwards we can compute the nuclear modification factor for the low p_T region. The improvement of the yield will be done using boosted decision trees.

[1] It is necessary to mention that the improvement was also due to the installation of the Heavy Ion Tracker detector.

References

[1] J. Kvapil. $D^{\pm}$ production in Au+Au collisions at $\sqrt{s_{\mathrm{NN}}} = 200$ GeV measured by the STAR experiment. Quark Matter Conference, 2017.

[2] A. Hoecker et al. TMVA 4: Toolkit for Multivariate Data Analysis with ROOT. Users Guide. 2013.

[3] M. Lomnitz. Measurement of D^0 elliptic and triangular flow in Au+Au collisions at $\sqrt{s_{NN}} = 200$ GeV at RHIC

Impact of invisible energy on the energy reconstruction of cosmic ray shower at the Pierre Auger Observatory

Šimon Novák*(novaksi1@fjfi.cvut.cz)*

The Pierre Auger Observatory located in Argentinian pampas is the world's largest experiment for high-energy cosmic ray showers detection. The observatory's hybrid detector consists of a 3000 km^2 array of 1660 Water Cherenkov Stations working in cooperation with 4 fluorescence detector stations with 24 fluorescence telescopes in total. Since the start of operation in 2004 the observatory has detected hundreds of events with primary particle energy exceeding 10^{20} eV and was able to answer some questions about the properties of the most energetic cosmic rays currently observed in the universe.

As a cosmic ray shower propagates through the atmosphere, number of particles is multiplied through hadronic and electromagnetic cascades until a maximum is reached. Majority of shower energy is deposited into the atmosphere mainly by electrons and positrons emerging from aforementioned electromagnetic cascades. Excited atmospheric molecules emit UV light which can be detected by fluorescence detectors and thus a quantity directly related to shower total energy is measured. This is called *calorimetric energy*. The rest of shower energy not detectable by fluorescence detectors is called *invisible (missing) energy* and is carried away mainly by shower muons and neutrions originating from decay of unstable particles. Total energy of a shower can be then calculated from detector signals when a correction accounting for the invisible energy is applied.

One way to estimate the missing energy of a shower is to calculate the mean missing energy parameter C_{miss} as a function of the calorimetric energy using MC simulations of showers with known parameters. The parameter C_{miss} is defined as follows

$$\langle C_{miss} \rangle = \frac{\langle E_{cal} \rangle}{E_0} = a - b \left(\frac{\langle E_{cal} \rangle}{1\text{EeV}} \right)^c , \tag{1}$$

where E_{cal} is shower calorimetric energy, E_0 is shower primary energy and a, b, c are parameters to be fitted from simulated showers. For this work, program CONEX with hadronic interaction models EPOS LHC and QGSJET-II-04 was used and 5600 showers with primary energies from 10^{17} eV to 10^{20} eV with primary particle either proton or iron nucleus were simulated. The calorimetric energy of every shower was calculated by fitting the shower's energy deposition profile by integrated Gaisser-Hillas function in the form

$$f_{GH}(X) = \frac{E_{cal}}{\lambda} \left(\frac{X - X_0}{\lambda} \right)^{\frac{X_{max} - X_0}{\lambda}} \exp\left(\frac{X_0 - X}{\lambda} \right) \left[\Gamma\left(\frac{X_{max} - X_0}{\lambda} + 1 \right) \right]^{-1} , \tag{2}$$

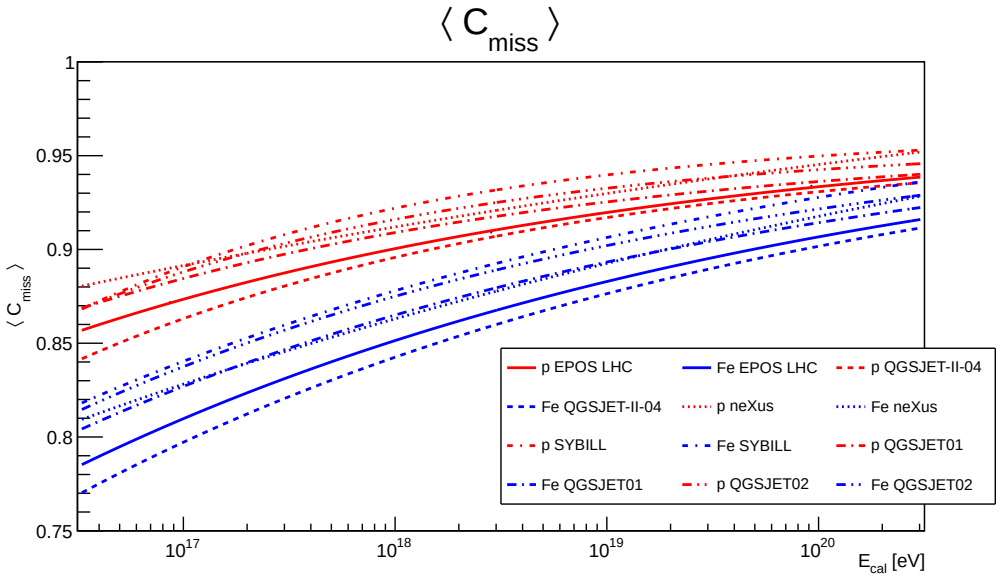

Figure 1: C_{miss} parameter as a function of the calorimetric energy shown for various interaction models and both primary particle types.

where X is atmospheric depth, X_{max} is the depth of shower maximum and X_0, λ are two more fit parameters.

Results of the C_{miss} parameter for simulated data together with results from the work [1] utilizing different interaction models are shown in Fig. 1. It is clear that the biggest missing energy portion is predicted by QGSJET-II-04 model followed by EPOS LHC. One could here take the average of C_{miss} parameters a, b, c for all shown hadronic interaction models and both primary particles and use this sole C_{miss} parametrization to calculate the total energy of a random cosmic ray shower with a priori unknown primary particle.

Another method for the missing energy estimation independent of chosen interaction models is to utilize the dependance of the missing energy on the overall number of muons in a shower. As can be seen in Fig. 2 there is linear dependance between logarithms of the two quantites, hence the information about the number of muons in a shower could be directly used for missing energy calculation event-by-event. Currently, measurement of muons in a shower at the PAO is unsufficient as the signal in surface detectors is proportional to both residual electromagnetic and muonic component of a shower hitting the ground.

By comparison of the two methods, one can see in the Fig. 3 showing histograms of total shower energy reconstruction errors that the C_{miss} method tends to overestimate missing energy in proton induced showers and underestimate it in iron induced shower. Clearly, this is a consequence of taking the C_{miss} parameter as an average. The reconstruction using the number of muons in a shower shows smaller error in shower energy reconstruction as the missing energy is calculated more precisely for every shower from its respective number of muons.

The AugerPrime upgrade currently underway at the PAO is also focused on improving the muon signal recognition in the SD stations by installing a 4 m^2 scintillators on top of each SD station. A better energy reconstruction could then be potentialy achieved by utilizing succesfully the event-by-event method. Studies in this direction are subject of

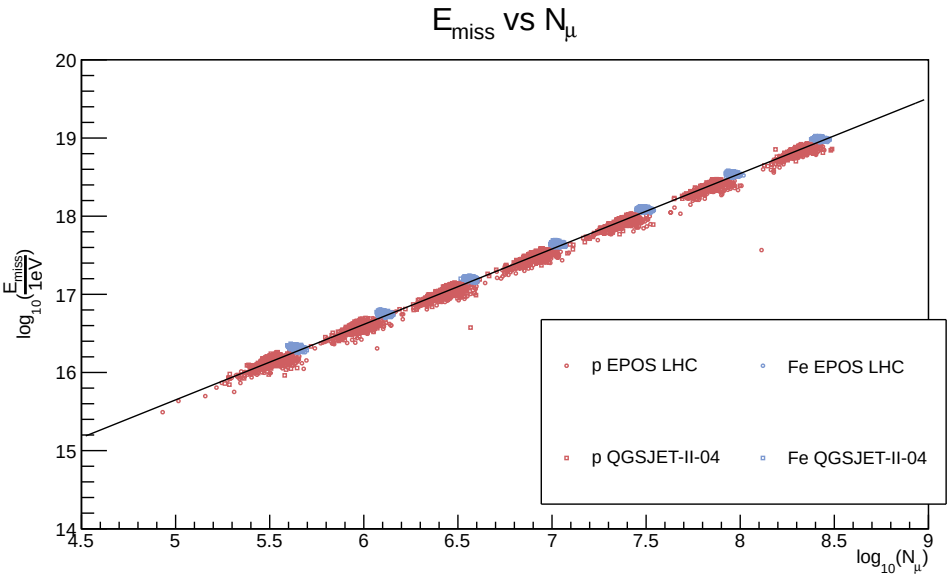

Figure 2: Missing energy of a shower plotted versus its respective number of muons (both in logarithm).

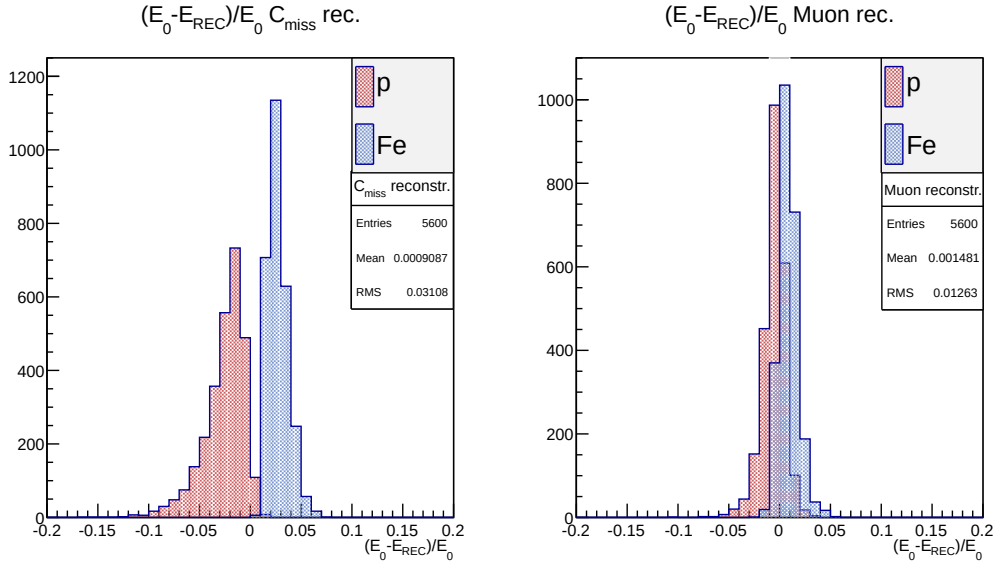

Figure 3: Comparison of errors in shower total energy calculation for simulated showers by two different methods.

author's further research.

References

[1] M. Nyklíček, J. Řídký and P. Trávníček, *Influence of hadronic interaction models on determination of chemical composition and size of the missing energy*, GAP notes (2008)

Experimental study of coincidence processes in microscopic quantum hardware generators of coincidence events

Tomas Novak*(novakt36@fjfi.cvut.cz)*

There are three different processes occuring in nature and two of them are closely related. The first one and independent of the other two is stochastic process, which takes place in microscopic quantum systems as a measurement of the system, or as a interaction of the system with its surroundings. The coincident result of the process cannot be predicted and even can lead to coincident behaviour of a macroscopic systems. Deterministic process is different, the result unambiguously depends on intial conditions and laws characterizing the process. Chaotic process is the extension of the deterministic one, where the complexity of the system prevent it from being practically predicted, but not in the theoretical manner. On the base of the results of the processes we can generating serieses of numbers which are obtained as a bijection between the results and the numbers.

Random number generators producing the time series and are based on one of the fundamental processes mentioned above. In general it is complicated to define an "amount of randomness" of the series and so it is neccesary to examine the source of the series.

Pseudorandom number generator is the deterministic approach and mostly used as a singleparametric resp. multiparametric computer algorithm, whererse the manifested series depends only on the intial parameters – the *seed*. Those generators are called "pseudo" because it is possible to find a correlations between values or prefered values of the series, also it is naturally periodic and possible to predicte. But because of the use of an *unbiasing algorithms* – which shuffles the serie and extension of the periodicity to reasonable size, those pseudorandom number generators are widely use in many applications with satisfying results.

Hardware random number generators are based on the chaotic processes as they are unable to be practically predicted and can be considered as the source of randomness. For example such a process can be a roulette. Chaos theory is mentioned later in the text and is trying to describe the chaotic processes and extract as much information as possible.

Most credible approach of generating random numbers seems to be quantum hardware random number generator. It exploits stochastic character of a measurement of observable variable of quantum system described by Born's rule. But in contrast with credibility

of this generator it was observed, that generated series is not always stationary – the distribution of possible values is not stationary.

Chaos theory study deterministic systems highly sensitive to intial conditions. Mostly focuses on non linear dynamical systems, but is also used interdisciplinary. Its main goal is to find *attractors* resp. *strange attractors* of the system in the phase space. To find appropriate phase space the methods and tools of the *non linear time series analysis* are exploited.

In my bachelor thesis I focus on non stationarity of time series obtained from measurement of observable variable of microscopic quantum system. Part of the time series when non stationarity occure is examined with methods and tools of non linear time series analysis of software package TISEAN.

References

[1] H. Kantz, T. Schreiber, Nonlinear time series analysis, 369 [online] `http://www.fulviofrisone.com/attachments/article/485/Nonlinear%20Time%20Series%20Analysis%20(Kantz,%20Schreiber)(Cambridge%202004)(2nd%20ed).pdf`

[2] Xiongfeng Ma, Xiao Yuan, Zhu Cao, Bing Qi, Zhen Zhang, Quantum random number generation, 9 [online] `https://www.nature.com/articles/npjqi201621`

Muon opposite side tagging in $B_S \to J/\psi + \phi$

Lukáš Novotný *(novotl23@fjfi.cvut.cz)*

1 CP Violation

In 1964, Christenson, Cronin, Fitch and Turlay observed the neutral K meson decay. They were studied eigenstates of two neutral K mesons, called short-lived and long-lived kaons (K_S^0 and K_L^0). If CP is conserved, the final states are only $K_S^0 \to 2\pi$ and $K_L^0 \to 3\pi$ and mass eigenstates are also CP eigenstates. However, K_L^0 also sometimes decays in 2 pions, which means the CP eigenstates are different from the mass eigenstates and the K^0 and $\bar{K}^0$ can oscillate into each other, thus the CP is violated.

1.1 Types of CP violation

There are three ways, how the CP can be violated - CP violation in decay, in mixing and in interference of mixing and decay.

The CP violation in decay (also know as direct CP violation) is the only possible source of CP asymmetry in charged meson decays. The decay amplitude of particle M into final state f is different from the decay amplitude of antiparticle into final antistate,

$$\Gamma\left(M \to f\right) \neq \Gamma\left(\bar{M} \to \bar{f}\right). \tag{1}$$

The CP violation in mixing (or indirect CP violation) arises when the probability of oscillation from meson to anti-meson is different from the probability of oscillation from anti-meson to meson,

$$\text{Prob}\left(P^0 \to \overline{P}^0\right) \neq \text{Prob}\left(\overline{P}^0 \to P^0\right) \tag{2}$$

Thus the mass eigenstates are not CP eigenstates.

The CP violation in interference of mixing and decay occurs in case both meson and antimeson decay into the same final state, $M^0 \to f$ and $M^0 \to \bar{M}^0 \to f$. This case occurs for example in the decay $B_s^0 \to J/\psi\phi$.

1.2 CP Violation in the Standard Model

The GIM mechanism (S. Glashow, I. Iliopoulos and L. Maiani) describing relation between interaction and mass eigenstates for two families of quarks was generalised to three families

by M. Kobayashi and K. Maskawa in 1973. The general quark mixing transformation with the unitary Cabibbo, Kobayashi, Maskawa (CKM) mixing matrix is

$$\begin{pmatrix} V_{ud} & V_{us} & V_{ub} \\ V_{cd} & V_{cs} & V_{cb} \\ V_{td} & V_{ts} & V_{tb} \end{pmatrix}. \tag{3}$$

Its element are used for evaluation of vertex factors in Feynman diagrams. This matrix is unitary, which leads to twelve distinct complex relations among the matrix elements. Six of them can represented geometrically as triangles in the complex plane. One of these relations is

$$V_{us}V_{ub}^{*} + V_{cs}V_{cb}^{*} + V_{ts}V_{tb}^{*} = 0. \tag{4}$$

The CP violating phase ϕ_s is defined as the weak phase difference between the $B_s^0 - \bar{B}_s^0$ mixing amplitude and the $b \to c\bar{c}s$ decay amplitude and is related to the angle of the triangle (4), thus

$$\phi_s = -2\beta_s = -2\text{arg}\left(\frac{V_{ts}V_{tb}^{*}}{V_{cs}V_{cb}^{*}}\right). \tag{5}$$

2 $B_s^0 \to J/\psi\phi$ analysis

2.1 Opposite side tagging

The CP violating phase defined in (5) can be measured in $B_s^0 \to J/\psi\phi$ decay. Before the ϕ_s determination, the b quark or antiquark in B_s^0 has to be identified. B meson at LHC are produced in the hadronization of the $b\bar{b}$ pair. One b quark (it is unknown, whether it is quark or antiquark) are used to form the B_s^0, and second one from the pair is used for the identification when decaying into jets, muon or electron. This method is referred to as opposite-side tagging (OST). However, the B meson formed by the second b quark can decay via the weak interaction and then decay into the jet, muon or electron, so the charge is not always same as the charge of the B meson. To optimize the tagging performance, a muon cone charge variable is constructed, defined (for muons) as

$$Q_\mu = \frac{\sum_i^{Ntracks} q_i \left(p_\mathrm{T}\right)^\kappa}{\sum_i^{Ntracks} \left(p_\mathrm{T}\right)^\kappa}, \tag{6}$$

where q_i is charge of the track, $\kappa = 1.1$ and the sum is performed over the reconstructed ID tracks within a cone $\Delta R = \sqrt{(\Delta\phi)^2 + (\Delta\eta)^2} < 0.5$ around the muon direction.

Events containing $B^\pm \to J/\psi + K^\pm$ decays are used to study and calibrate the OST methods. The initial flavour in this decay is known and then the tag-probability for each B_s^0 candidate is determined from calibrations of $B^\pm$ candidates sample.

2.2 From $B^\pm$ to B_s^0 tag probability

Using the OST, the probability distribution can be obtained. This distribution for combined muons with $|Q_\mu| < 1$ in Run1, often called as the calibration curve, can be seen in Figure 1. The muon cone charge distribution in $B_s^0 \to J/\psi\phi$ can be then transformed with this calibration curve in to the Bs tag probability (Figure 2). The signal and background

part of this distribution is then fitted and both fitted functions are used in the fullfit code as Punzi terms. The fullfit code fit the $B_s^0 \to J/\psi\phi$ decay rate, where also the weak phase ϕ_s (5) is one of the fitted parameter.

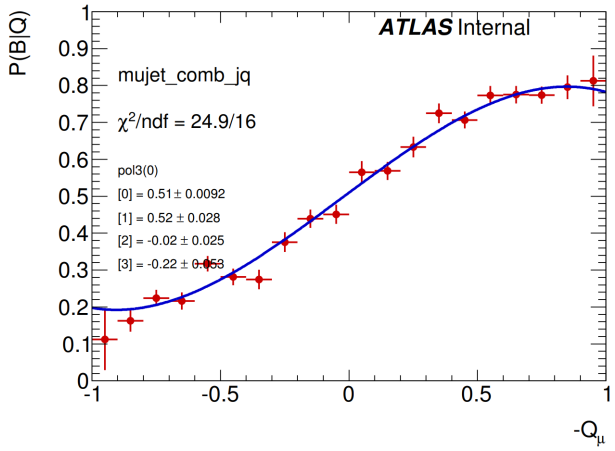

Figure 1: $B^{\pm} \to J/\psi + K^{\pm}$ tag probability distribution (calibration curve) in dependence on muon cone charge.

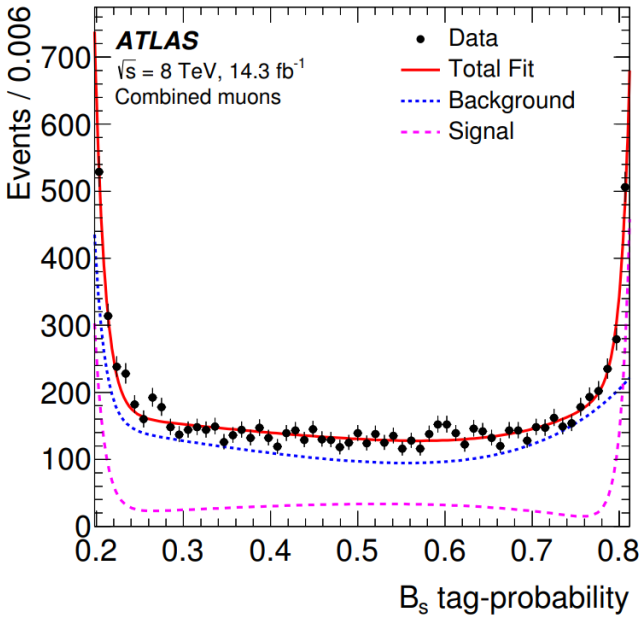

Figure 2: $B_s^0 \to J/\psi\phi$ tag probability distribution.

References

[1] G. Aad, et al. Measurement of the CP-violating phase ϕ_s and the B_s^0 meson decay width difference with $B_s^0 \to J/\psi\phi$ decays in ATLAS. JHEP 08:147, (2016)

Search for BsPi resonance

Radek Novotny *(Radek.Novotny2@fjfi.cvut.cz)*

In early 2016, the DØ [1]collaboration announced the observation of narrow structure referred to as X(5568), in $B_s^0\pi^\pm$ spectrum in $p\bar{p}$ collisions at $\sqrt{s} = 1.96$ TeV center-of-mass energy. The most probable explanation of such as exotic state would be the hadron composed of four quarks (b, s, u, d). This exotic state would be very important for the understanding of production mechanism of multiquark objects and in the case of the tightly bound di-quark anti-diquark pair, this may provide an additional information to strong interaction.

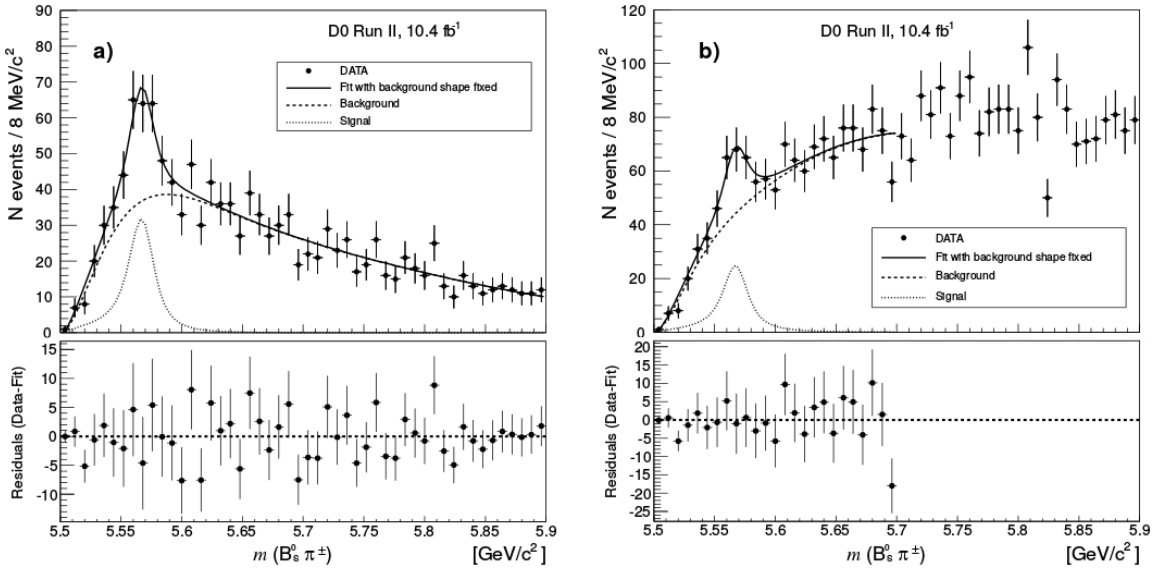

Figure 1: The $m(B_s^0\pi^\pm)$ distribution together with the background distribution and the fit results (a) after applying the cone cut and (b) without the cone cut.[1]

The promising result from DØ collaboration was further investigated by other two collaborations LHCb and CMS. Because both of these experiments do not see any evidence of the claimed state $X(5568)$ they published the upper limit on 95% CL of relative production rate of $B_s^0\pi^\pm$ to B_s^0, which is defined as

$$\rho_X \equiv \frac{\sigma(pp \to X + \text{anything}) \times \mathcal{B}(X \to B_s^0\pi^\pm)}{\sigma(pp \to B_s^0 + \text{anything})}, \tag{1}$$

$$= \frac{N(X)}{N(B_s^0)} \times \frac{1}{\epsilon^{\text{rel}}(X)}, \tag{2}$$

where the σ are the cross-sections related to the produced particles within the detector acceptance and $\epsilon^{\rm rel}(X)$ is a relative efficiency of the $B_s^0\pi^\pm$ state X and the B_s^0 meson.

The CMS [2] collaboration set the upper limit using two different cuts on B_s transverse momenta to the values of $\rho_{\rm X}(p_T(B_s^0) > 10$ GeV$) < 1.0\%$ at 95% CL and $\rho_{\rm X}(p_T(B_s^0) > 15$ GeV$) < 1.1\%$ at 95% CL

The LHCb [3] collaboration made more complex study and set the upper limit for D$\emptyset$ values in three cuts on $p_{\rm T}(B_s^0)$

$$\rho_X^{\rm LHC}{}^b(p_{\rm T}(B_s^0) > 5 \text{ GeV}) < 0.012,$$
$$\rho_X^{\rm LHC}{}^b(p_{\rm T}(B_s^0) > 10 \text{ GeV}) < 0.024,$$
$$\rho_X^{\rm LHC}{}^b(p_{\rm T}(B_s^0) > 15 \text{ GeV}) < 0.020.$$

They have also made a mass scans over the region below the 6000 MeV using the 10 MeV steps and varying the width of resonance from 10 to 50 MeV with the same conclusion that there is no significant excess in the $B_s^0\pi^\pm$ spectrum.

The ATLAS [4] collaboration made study of the BsPi resonance in the simmilar kinematic region as CMS using all data from RUN 1 with total luminosity of $\sim$ 25 fb^{-1}. From preliminary results can be seen that there is no significant excess in the $B_s^0\pi^\pm$ spectrum in the claimed region and all results are with agreement with background only hypothesis within two sigma region. The most imortant steps in the ALTAS analysis were presented and fast insight into advanced statistical tools was made.

References

[1] V. M. Abazov, et al. Evidence for a $B_s^0\pi^\pm$ state. *Phys Rev Lett* **117**(2):022003, 2016. 1602.07588.

[2] A. M. Sirunyan *et al.* [CMS Collaboration], "Search for the X(5568) state decaying into $\rm B_s^0\pi^\pm$ in proton-proton collisions at $\sqrt{s} = 8$ TeV," arXiv:1712.06144 [hep-ex].

[3] R. Aaij, et al. Search for Structure in the $B_s^0\pi^\pm$ Invariant Mass Spectrum. *Phys Rev Lett* **117**(15):152003, 2016. 1608.00435.

[4] M. Aaboud *et al.* [ATLAS Collaboration], "Search for a Structure in the $B_s^0\pi^\pm$ Invariant Mass Spectrum with the ATLAS Experiment," arXiv:1802.01840 [hep-ex].

Coupling of Λ to Atomic Nuclei

Jan Pokorný *(pokorny@ujf.cas.cz)*

1 Introduction

Theoretical nuclear physics deals with two main issues - the first, the description of the force acting among nucleons, the second, the application of this force in quantum many-body methods.

The nucleon-nucleon (NN) potentials can be divided into two classes - effective and realistic. Effective NN potentials rely on sets of parameters which are directly fitted to the bulk properties of doubly magic nuclei. Examples of effective potentials are the Skyrme [1] and Gogny [2] forces. Realistic (or high-precision) NN potentials are derived from the microscopic theory of NN scattering and reproduce the experimental phase shifts. They are either derived from the idea of meson exchanges (Nijmegen [3], Argonne V18 [4], CD-Bonn [5]), or from the Chiral Perturbation Theory (ChPT). The ChPT is an effective field theory which satisfies the symmetries of the QCD and adopts nucleons and pions as the degrees of freedom [6, 7]. The perturbative character of the ChPT allows to improve the precision of the NN potential by going into higher order of pertubation. Starting from the next-to-next-to leading order ($\mathrm{N^2LO}$), the three-body NNN interactions appear.

Heavier nuclei with $A \gtrsim 10$ are described by the mean-field models, e.g. models based on the Hartree-Fock (HF) method. In this work, we obtain the nuclear mean-field by solving the HF method with the two-body and three-body interactions. We implement the chiral $\mathrm{N^2LO}$ potential with explicit NN and NNN interactions with parametrization $\mathrm{NNLO_{sat}}$ [8].

Theory of nuclear structure can be extended to exotic nuclear systems, such as hypernuclei. A hypernucleus is an exotic nuclear system which consists of protons, neutrons and hyperons (e.g. $\Lambda, \Sigma, \Xi, \Omega$). Hyperons (with exception of Σ^0) decay predominantly weakly which results in their long lifetime ($\approx 10^{-10}$ s) compared to the time scale of the strong interaction ($\approx 10^{-23}$ s). This allows experimental study of hypernuclei, including their structure. Moreover, the hyperons bound in nuclear medium are not affected by Pauli exclusion principle from nucleons which makes them unique probes of the nuclear interior. Experimental and theoretical study of hypernuclei contributes to our better understanding of nuclear structure and baryon-baryon forces.

First hypernucleus was observed in nuclear emulsion exposed to cosmic rays (Danysz, Pniewski 1953 [9]). Since then, hypernuclei have been studied experimentally using emulsion detectors, first with cosmic rays, and later with particles from accelerators. In recent years, the technical advent of the particle accelerators and detectors has increased the rate and depth of the experimental investigation of strangeness in nuclei. Theoretical studies

closely follow the experimental development [10]. Hypernuclei can be theoretically studied using conventional methods of nuclear physics accompanied by the implementation of the ΛN interaction. Several hyperon-nucleon (YN) potentials, both bare and effective, have been developed for such purpose and chiral YN interaction at the LO [14]. In our model we implement the ΛN channel of the chiral LO YN interaction with cutoff $\lambda = 550$ MeV.

In this work, we study the effect of the three-body NNN interactions on properties of given single-Λ hypernuclei and their respective nuclear cores. We extend the hypernuclear mean-field model that has been introduced in Ref. [13]. We implement the chiral $\mathrm{NNLO_{sat}}$ NN + NNN potential [8] and the chiral LO ΛN potential [14].

2 Hartree-Fock method

We describe the single-Λ hypernucleus as a many-body system consisting of the nuclear core and one Λ hyperon. Properties of the hypernucleus are determined by the Hamiltonian

$$\widehat{H} = \widehat{T}^N + \widehat{T}^\Lambda + \widehat{V}^{NN} + \widehat{V}^{NNN} + \widehat{V}^{\Lambda N} + \widehat{V}^{\Lambda NN} - \widehat{T}_{CM}. \tag{1}$$

Here, $\widehat{T}^N$ and $\widehat{T}^\Lambda$ denote the sums over kinetic operators of nucleons and the Λ particle, respectively. The terms $\widehat{V}^{NN}$ and $\widehat{V}^{\Lambda N}$ stand for sums over the two-body NN and ΛN potentials. Sums over the three-body interactions are included in the terms $\widehat{V}^{NNN}$ and $\widehat{V}^{\Lambda NN}$. The term $\widehat{T}_{CM}$ denotes the center-of-mass kinetic operator

$$\widehat{T}_{CM} = \frac{1}{2M(A+0.19)} \left(\sum_{a=1}^{A} \widehat{\vec{P}}_a^{\,2} + 2 \sum_{a<b} \widehat{\vec{P}}_a \cdot \widehat{\vec{P}}_b \right), \tag{2}$$

where $M \approx 938$ MeV is the mass of a nucleon, A is the baryon number, and $\widehat{\vec{P}}_a$ is the momentum operator of the a-th particle. Here we use the fact that mass of the Λ hyperon is approximately $M_\Lambda \approx 1.19M$.

The hypernuclear mean field is constructed self-consistently by the Hartree-Fock (HF) method. We derive the HF method for a system of identical fermions with the two-body interactions in the formalism of the second quantization. We show the HF method for the single-Λ hypernuclei including the three-body NNN and the ΛNN interactions in the proton-neutron-Λ (pnΛ) formalism.

In the pnΛ formalism, the protons are represented by the creation (annihilation) operators $a^\dagger(a)$, neutrons by $b^\dagger(b)$, and the Λ by the $c^\dagger(c)$. We define the HF ground state as

$$|\mathrm{HF}\rangle = \prod_{i=1}^{Z} a_i^\dagger |0\rangle \otimes \prod_{i=1}^{N} b_i^\dagger |0\rangle \otimes c_1^\dagger |0\rangle. \tag{3}$$

The Hartree-Fock method is a variational method that minimizes the functional

$$E_{\mathrm{HF}} = \langle \mathrm{HF}|\widehat{H}|\mathrm{HF}\rangle. \tag{4}$$

We obtain three sets of HF equations. The HF equation for protons:

$$\begin{aligned} t^{\mathrm{p}}_{ij} + \sum_{kl} V^{\mathrm{pp}}_{ikjl}\rho^{\mathrm{p}}_{lk} + \sum_{kl} V^{\mathrm{pn}}_{ikjl}\rho^{\mathrm{n}}_{lk} + \sum_{kl} V^{\mathrm{p}\Lambda}_{ikjl}\rho^{\Lambda}_{lk} + \frac{1}{2}\sum_{klmn} V^{\mathrm{ppp}}_{ikljmn}\rho^{\mathrm{p}}_{mk}\rho^{\mathrm{p}}_{nl} \\ + \frac{1}{2}\sum_{klmn} V^{\mathrm{pnn}}_{ikljmn}\rho^{\mathrm{n}}_{mk}\rho^{\mathrm{n}}_{nl} + \sum_{klmn} V^{\mathrm{ppn}}_{ikljmn}\rho^{\mathrm{p}}_{mk}\rho^{\mathrm{n}}_{nl} + \sum_{klmn} V^{\mathrm{pp}\Lambda}_{ikljmn}\rho^{\mathrm{p}}_{mk}\rho^{\Lambda}_{nl} \\ + \sum_{klmn} V^{\mathrm{pn}\Lambda}_{ijklmn}\rho^{\mathrm{n}}_{mk}\rho^{\Lambda}_{nl} = \varepsilon^{\mathrm{p}}_{i}\delta_{ij}. \end{aligned} \tag{5}$$

The HF equation for neutrons:

$$\begin{aligned} t^{\mathrm{n}}_{ij} + \sum_{kl} V^{\mathrm{nn}}_{ikjl}\rho^{\mathrm{n}}_{lk} + \sum_{kl} V^{\mathrm{pn}}_{kilj}\rho^{\mathrm{p}}_{lk} + \sum_{kl} V^{\mathrm{n}\Lambda}_{ikjl}\rho^{\Lambda}_{lk} + \frac{1}{2}\sum_{klmn} V^{\mathrm{nnn}}_{ikljmn}\rho^{\mathrm{n}}_{mk}\rho^{\mathrm{n}}_{nl} \\ + \frac{1}{2}\sum_{klmn} V^{\mathrm{ppn}}_{klimnj}\rho^{\mathrm{p}}_{mk}\rho^{\mathrm{p}}_{nl} + \sum_{klmn} V^{\mathrm{pnn}}_{klimnj}\rho^{\mathrm{p}}_{mk}\rho^{\mathrm{n}}_{nl} + \sum_{klmn} V^{\mathrm{nn}\Lambda}_{ikljmn}\rho^{\mathrm{n}}_{mk}\rho^{\Lambda}_{nl} \\ + \sum_{klmn} V^{\mathrm{pn}\Lambda}_{klimnj}\rho^{\mathrm{p}}_{mk}\rho^{\Lambda}_{nl} = \varepsilon^{\mathrm{n}}_{i}\delta_{ij}. \end{aligned} \tag{6}$$

The HF equation for the Λ particle:

$$\begin{aligned} t^{\Lambda}_{ij} + \sum_{kl} V^{\mathrm{p}\Lambda}_{kilj}\rho^{\mathrm{p}}_{lk} + \sum_{kl} V^{\mathrm{n}\Lambda}_{kilj}\rho^{\mathrm{n}}_{lk} + \frac{1}{2}\sum_{klmn} V^{\mathrm{pp}\Lambda}_{klimnj}\rho^{\mathrm{p}}_{mk}\rho^{\mathrm{p}}_{nl} + \frac{1}{2}\sum_{klmn} V^{\mathrm{nn}\Lambda}_{klimnj}\rho^{\mathrm{n}}_{mk}\rho^{\mathrm{n}}_{nl} \\ + \sum_{klmn} V^{\mathrm{pn}\Lambda}_{klimnj}\rho^{\mathrm{p}}_{mk}\rho^{\mathrm{n}}_{nl} = \varepsilon^{\Lambda}_{i}\delta_{ij}. \end{aligned} \tag{7}$$

3 Tamm-Dancoff Approximation, NΛ-TDA

The $|\mathrm{HF}\rangle$ state does not give a good description of the wave function of the hypernuclear ground state. We need to take into account also the correlations from particle-hole excitations of the nuclear core. The particle-hole excitations (phonons) can be described by the Tamm-Dancoff Approximation (TDA). We generalized this method to the NΛ-TDA which couples the Λ particle in a given particle state to a proton or neutron hole state. This allows us to describe hypernuclei with even-odd or odd-even nuclear cores.

The NΛ TDA phonon operators are defined as

$$R^{\dagger}_{\mu,\mathrm{p}\Lambda} = \sum_{ph} r^{\mu,\mathrm{p}\Lambda}_{ph} c^{\dagger}_{p} a_{\overline{h}}, \tag{8a}$$

$$R^{\dagger}_{\mu,\mathrm{n}\Lambda} = \sum_{ph} r^{\mu,\mathrm{n}\Lambda}_{ph} c^{\dagger}_{p} b_{\overline{h}}. \tag{8b}$$

The equations of motion of the NΛ TDA method are again formulated in analogy to the TDA:

$$\langle \mathrm{HF}|R_{\nu',\mathrm{p}\Lambda}[\widehat{H}, R^{\dagger}_{\nu,\mathrm{p}\Lambda}]|\mathrm{HF}\rangle = (E^{\mathrm{p}\Lambda}_{\nu} - E_{\mathrm{HF}})\delta_{\nu\nu'}, \tag{9a}$$

$$\langle \mathrm{HF}|R_{\nu',\mathrm{n}\Lambda}[\widehat{H}, R^{\dagger}_{\nu,\mathrm{n}\Lambda}]|\mathrm{HF}\rangle = (E^{\mathrm{n}\Lambda}_{\nu} - E_{\mathrm{HF}})\delta_{\nu\nu'}. \tag{9b}$$

By inserting the Hamiltonian $\widehat{H}$ as a sum of terms $E_{\rm HF}, \widehat{H}^{(1)}, \widehat{H}^{(2)}$, and $\widehat{H}^{(3)}$, we evaluate the commutation relations $[\widehat{H}, R^{\dagger}_{\nu,{\rm p}\Lambda}]$ and $[\widehat{H}, R^{\dagger}_{\nu,{\rm n}\Lambda}]$ term by term,

$$[E_{\rm HF}, R^{\dagger}_{\nu,{\rm p}\Lambda}]|{\rm HF}\rangle = 0, \tag{10a}$$
$$[E_{\rm HF}, R^{\dagger}_{\nu,{\rm n}\Lambda}]|{\rm HF}\rangle = 0, \tag{10b}$$

$$[\widehat{H}^{(1)}, R^{\dagger}_{\nu,{\rm p}\Lambda}]|{\rm HF}\rangle = \sum_{ph}(\varepsilon^{\Lambda}_{p} - \varepsilon^{\rm p}_{h}) r^{\nu,{\rm p}\Lambda}_{ph} c^{\dagger}_{p} a_{\overline{h}}|{\rm HF}\rangle, \tag{11a}$$
$$[\widehat{H}^{(1)}, R^{\dagger}_{\nu,{\rm n}\Lambda}]|{\rm HF}\rangle = \sum_{ph}(\varepsilon^{\Lambda}_{p} - \varepsilon^{\rm n}_{h}) r^{\nu,{\rm n}\Lambda}_{ph} c^{\dagger}_{p} b_{\overline{h}}|{\rm HF}\rangle, \tag{11b}$$

$$[\widehat{H}^{(2)}, R^{\dagger}_{\nu,{\rm p}\Lambda}]|{\rm HF}\rangle = -\sum_{p_1h_1}\sum_{ph} \overline{V}^{{\rm p}\Lambda,{\rm gen}}_{\overline{h}p_1h_1p} c^{\dagger}_{p_1} a_{h_1}|{\rm HF}\rangle, \tag{12a}$$
$$[\widehat{H}^{(2)}, R^{\dagger}_{\nu,{\rm n}\Lambda}]|{\rm HF}\rangle = -\sum_{p_1h_1}\sum_{ph} \overline{V}^{{\rm n}\Lambda,{\rm gen}}_{\overline{h}p_1h_1p} c^{\dagger}_{p_1} b_{h_1}|{\rm HF}\rangle. \tag{12b}$$

Again, it applies that

$$\langle {\rm HF}|R_{\nu',{\rm p}\Lambda}[\widehat{H}^{(3)}, R^{\dagger}_{\nu,{\rm p}\Lambda}]|{\rm HF}\rangle = \langle {\rm HF}|R_{\nu',{\rm n}\Lambda}[\widehat{H}^{(3)}, R^{\dagger}_{\nu,{\rm n}\Lambda}]|{\rm HF}\rangle = 0. \tag{13a}$$

The substitution of the Eqs. (11a) and (12a) into Eq. (9a) (and Eqs. (11b) and (12b) into Eq. (9b)) leads to

$$\langle {\rm HF}|R_{\nu',{\rm p}\Lambda}[\widehat{H}, R^{\dagger}_{\nu,{\rm p}\Lambda}]|{\rm HF}\rangle = \sum_{ph}\sum_{p'h'} r^{\nu',{\rm p}\Lambda}_{p'h'} r^{\nu,{\rm p}\Lambda}_{ph} \left((\varepsilon^{\Lambda}_{p} - \varepsilon^{\rm p}_{h})\delta_{pp'}\delta_{hh'} - \overline{V}^{{\rm p}\Lambda,{\rm gen}}_{\overline{h}p'\overline{h}'p} \right), \tag{14a}$$
$$\langle {\rm HF}|R_{\nu',{\rm n}\Lambda}[\widehat{H}, R^{\dagger}_{\nu,{\rm n}\Lambda}]|{\rm HF}\rangle = \sum_{ph}\sum_{p'h'} r^{\nu',{\rm n}\Lambda}_{p'h'} r^{\nu,{\rm n}\Lambda}_{ph} \left((\varepsilon^{\Lambda}_{p} - \varepsilon^{\rm n}_{h})\delta_{pp'}\delta_{hh'} - \overline{V}^{{\rm n}\Lambda,{\rm gen}}_{\overline{h}p'\overline{h}'p} \right). \tag{14b}$$

Eqs. (14a) and (14b) correspond to the following eigenvalue problems:

$$\sum_{ph} \left((\varepsilon^{\Lambda}_{p} - \varepsilon^{\rm p}_{h})\delta_{pp'}\delta_{hh'} - \overline{V}^{{\rm p}\Lambda,{\rm gen}}_{\overline{h}p'\overline{h'}p} \right) r^{\nu,{\rm p}\Lambda}_{ph} = (E^{{\rm p}\Lambda}_{\nu} - E_{\rm HF}) r^{\nu,{\rm p}\Lambda}_{p'h'}, \tag{15a}$$
$$\sum_{ph} \left((\varepsilon^{\Lambda}_{p} - \varepsilon^{\rm n}_{h})\delta_{pp'}\delta_{hh'} - \overline{V}^{{\rm n}\Lambda,{\rm gen}}_{\overline{h}p'\overline{h'}p} \right) r^{\nu,{\rm n}\Lambda}_{ph} = (E^{{\rm n}\Lambda}_{\nu} - E_{\rm HF}) r^{\nu,{\rm n}\Lambda}_{p'h'}. \tag{15b}$$

In practice, $\overline{V}^{{\rm p(n)}\Lambda,{\rm gen}}_{ijkl} \equiv \overline{V}^{{\rm p(n)}\Lambda}_{ijkl}$. We have developed a mathematical formalism of the NΛ TDA method which includes the three-body ΛNN interactions but we have not implemented the ΛNN interactions themselves in the numerical calculations. Here, we study the indirect effect of the NNN force which is accounted for in the HF calculations of the nuclear core (i.e. construction of the self-consistent basis).

4 Conclusions

We describe hypernuclei with even-even nuclear core and one valence Λ hyperon with the Hartree-Fock method. The HF method creates the hypernuclear mean field from the realistic chiral NN + NNN potential N^2LO_{sat} and from the ΛN channel of the chiral YN LO potential. This mean field is then used as a starting point for the Tamm-Dammcoff Approximation. The TDA couples particle-hole excitations (phonons) of the nuclear core. We generalized the TDA to NΛ-TDA which couples the Λ particle with a proton (or neutron) hole state. This allows us to describe hypernuclei with even-odd or odd-even nuclear cores. Results of the mentioned calculations for ^{16}O, $^{17}_{\Lambda}$O, $^{16}_{\Lambda}$O, $^{16}_{\Lambda}$N ^{40}Ca, $^{41}_{\Lambda}$Ca, $^{40}_{\Lambda}$Ca, $^{40}_{\Lambda}$K, ^{48}Ca, $^{49}_{\Lambda}$Ca, $^{48}_{\Lambda}$Ca, and $^{48}_{\Lambda}$K will be presented in the diploma thesis of the author of this text.

References

[1] T. H. R. Skyrme, Nucl. Phys. **9**, 615 (1959).

[2] J. Decharge, D. Gogny, Phys. Rev. C **21**, 1568 (1980).

[3] R. B. Wiringa, V. G. J. Stoks, R. Schiavilla, Phys. Rev. C **51** (1995).

[4] V. G. J. Stoks, R. A. M. Klomp, C. P. F. Terheggen, J. J. Swart, Phys. Rev. C **49**, 2950 (1994).

[5] R. Machleidt, F. Sammarruca, Y. Song, Phys. Rev. C **53** R1483 (1996).

[6] D.R. Entem, R. Machleidt, Phys. Lett. B, **524**, 1 (2002).

[7] R. Machleidt, D.R. Entem, Phys. Rep., **503**, 1 (2011).

[8] A. Ekström, G. R. Jansen, K. A. Wendt, G. Hagen, T. Papenbrock, B. D. Carlsson, C. Forssen, M. Hjorth-Jensen, P. Navratil, W. Nazarewicz, Phys. Rev. C **91**, 051301(R) (2015).

[9] M. Danysz, J. Pniewski, The London, Edinburgh, and Dublin Philosophical Magazine and Journal of Science, **44** 350 (1953).

[10] A. Gal, J. Mareš, *Topics in Strangeness Nuclear Physics*, Springer (2007).

[11] D. Bianco, F. Knapp, N. Lo Iudice, P. Vesely, F. Andreozzi, G. De Gregorio, A. Porrino, J. Phys. G: Nucl. Part. Phys. **41**, 025109 (2014).

[12] F. Knapp, N. Lo Iudice, P. Vesely, F. Andreozzi, G. De Gregorio, A. Porrino, Phys. Rev. C **92**, 054315 (2015).

[13] P. Vesely, E. Hiyama, J. Hrtankova, J. Mares, Nucl. Phys. A **954**, 260 (2016).

[14] H. Polinder, J. Haidenbauer, U. Meißner, Nucl. Phys. A **779**, 244 (2006).

Introduction to accelerator physics - Betatron oscillations

Ondřej Sedláček *(Sedlaon4@fjfi.cvut.cz)*

1 Introduction

For proper running and analyzing of high energy physics experiments knowledge of behavior of particle beam is essential. Accelerator physics study and measure among other things the properties of accelerated and collided beams of particles. One of the cornerstone of accelerator physics is called betatron oscillations and describes transverse dynamics of the accelerated particles.

2 Coordinate system

In accelerator physics Cartesian coordinate system is rarely used, since important formulas have complicated form in this coordinate system. Two different coordinates are common for longitudinal direction[1] and two pairs for transverse direction[2]. All these coordinates can be seen in Figure 1.

Two coordinates used for describing longitudinal direction are Θ and s. Θ is longitudinal phase, has dimension of angle and values from 0 to 2π, since Θ has relative nature it is commonly used for graphs and description where it is useful to avoid dimension of the accelerator, for example to express fractions of length of accelerator. s has dimension of length (meters, kilometers, etc.) and has direction of the beampipe and therefore is often used in formulas [1].

For transverse direction x and y or v and h is commonly used. v denotes vertical direction and h horizontal. x and y has the same meaning also denoting vertical and horizontal direction and usually x is equivalent to v and y to h, but the difference is that x and y are usually used when horizontal and vertical direction is exchangeable.

3 Betatron oscillations

In an accelerator a lot of particles are accelerated and because it is not possible to have all particles with exactly same initial properties at exact same position *Reference trajectory* is introduced. Reference trajectory, also called *Ideal trajectory*, is used for describing and calculating dynamics of the particles.

[1] Direction along the accelerating tube.

[2] Direction perpendicular to the accelerating tube

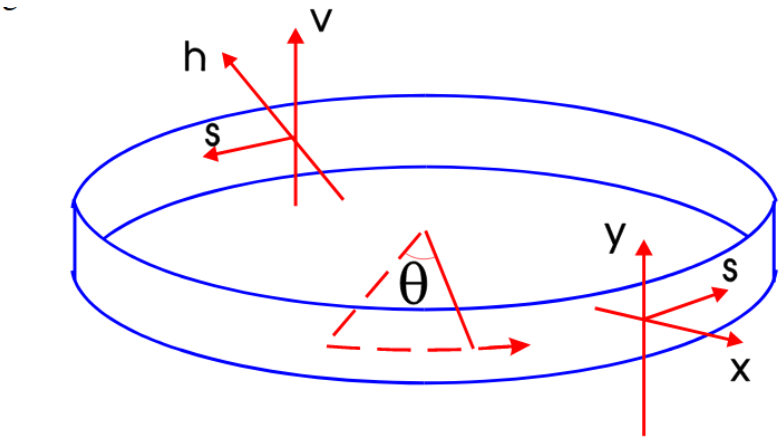

Figure 1: Scheme of coordinate systems used in accelerator physics. Source: [1].

Unideal particles, i.e. particles with different initial momentum, follow unideal trajectory. Difference in a transverse component of initial momentum leads to displacement of the particles relative to ideal trajectory. Magnets are used to close this unideal trajectories so particles are not lost, but this closing produces oscillatory motion of the particles around the ideal trajectory in the transverse plane. This relative motion of particles is called *Betatron oscillation* and forms the basis of all transverse motion in the accelerator [1]. As can be imagined, closing the trajectories and reducing amplitude of this oscillations while accelerating is desirable and is called focusing.

Dipole magnets are used for creating a *stable* (closed) trajectory in the horizontal plane (trajectory visualized in Figure 1), but in the history dipole magnets were also used for focusing. Focusing using dipole magnets is called *Weak focusing* and has a number of cons. Biggest disadvantage of weak focusing is low frequency and big amplitude of betatron oscillations and therefore large magnets and beam pipes are required.

Strong focusing is now largely used because it allows to reduce the size of beampipe and therefore used magnets. Strong focusing is done by using quadrupole magnets which focus in one direction (horizontal or vertical) and defocus in the other one, therefore series of mutually rotated quadrupole magnets is used. Cornerstone of this series is called *FODO cell* which consist of two quadrupole magnets (mutually rotated by 90°) and two drift spaces (Scheme in the Figure 2). Parameters of FODO cell are calculated in a way that the particles remain in the beampipe and the amplitudes of betatron oscillations are being reduced.

Betatron oscillations are similar to Linear Harmonic Oscillator which can be seen in the shape of equation of transverse motion of the particles called Hills equation [1]:

$$\frac{d^2x}{ds^2} + K(s)x = 0, \tag{1}$$

where x is displacement in transverse direction of the particles relative to the ideal trajectory and $K(s)$ is focusing strength of used magnets. Solution and approximate derivative for slowly changing focusing strength $K(s)$ has form [1]:

$$x = \sqrt{\epsilon\beta(s)}\cos(\Psi(s) + \Phi), x' = \sqrt{\frac{\epsilon}{\beta(s)}}\sin(\Psi(s) + \Phi) \tag{2}$$

where Φ is initial phase, $\Psi(s)$ phase is called *Phase advance* and depends on focusing strength, $\beta(s)$ is called *Beta function* and describes amplitude modulation due to the changing focusing strength and ϵ is constant called *Transverse emittance* if the described particle is on the *Envelope* of the beam (i.e. most particles has lower maximum amplitude) [1].

Emittance can also be defined as area in phase space filled if all particle are displayed in one figure as can be seen in the Figure 2. As well it is possible to define X% emittance where X is percentage of particle with lowest maximum amplitude included (e.g. 90% emittance is area in phase space filled by 90% of particles with lowest maximum amplitude and so on) [1]. The importance of emittance is that it is solely determined by initial conditions and remain constant as Liouville's theorem tells [2]. In particular the theorem says that the area in phase space remain constant under conservative force. This theorem is the reason why parameters of a particle source and first accelerator in accelerator cascade is very important.

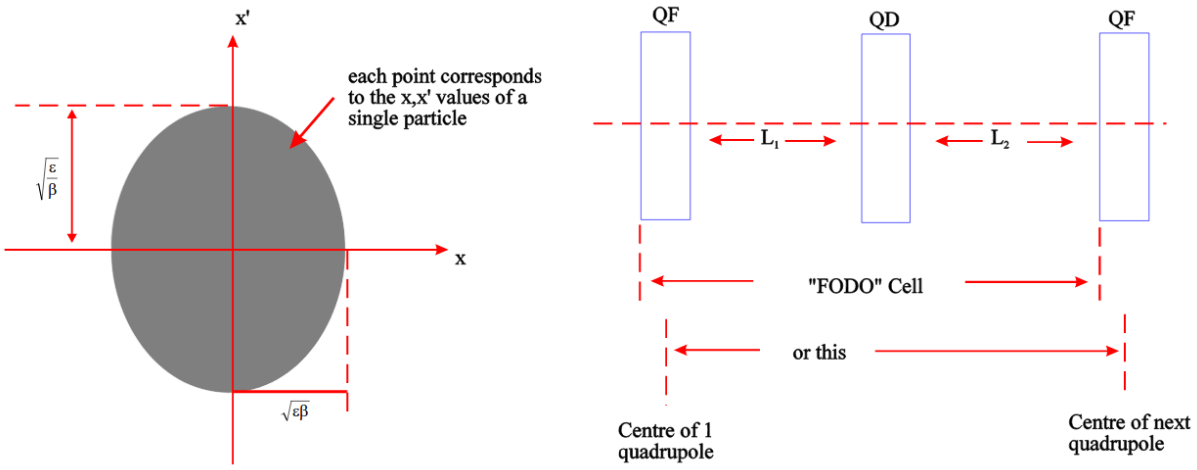

Figure 2: Scheme of a FODO cell (right) and emittance representation in phase space (left) Source: [1].

References

[1] S. Baird, Phys. Rep. 014, Accelerators for pedestrians (2007)

[2] Harald J.W. Müller-Kirsten, Basics of Statistical Physics, 2nd ed., World Scientific (Singapore, 2013)

Λ_c baryon reconstruction in Au+Au collisions at $\sqrt{s_{NN}} = 200$ GeV

Miroslav Šimko*(simko@ujf.cas.cz)*

The Λ_c baryon [2] is the lightest baryon containing the charm quark. As such, it presents a unique probe into the behavior of the, so called, strongly-coupled quark-gluon plasma (sQGP), produced in the the heavy-ion collisions at RHIC and the LHC.

Baryons have already proven to be excellent indicators of the behavior of sQGP. An enhancement of baryons compared to mesons is observed in the intermediate transverse momentum (p_T) range in central heavy-ion collisions [3]. This phenomenon is known as baryon enhancement and is believed to be one of the key pieces of evidence of the existence of the sQGP itself. This behavior can be explained via hadronization models which include quark coalescence, which is a process in which the quarks are combined to form hadrons, as compared to the quark fragmentation, in which new quarks are created from the vacuum.

The baryon enhancement observed at RHIC is demonstrated in Figure 1, in which the left-hand-side panel shows the ratio of the yield of p and $\overline{\mathrm{p}}$ to π^+ and π^-, and the middle panel is a plot of the ratio of Λ^+ and $\overline{\Lambda}^-$ to 2-times the yield of K^0_s. An enhancement in the p_T region of $\sim$2–4 GeV/c is clearly observed in the case of the Λ baryons. The plot in the right-hand-side panel shows theoretical estimates of the ratio of the yields of Λ_c to D^0. The scenario with no coalescence is demonstrated by the green line which was produced using the PYTHIA simulator [5]. The Statistical Hadronization Model (SHM), which calculates the ratios of particles using only the temperature and the volume of the system, is demonstrated by the gray rectangle [6]. This model has been extremely successful at predicting the ratios of light-flavor hadrons. The dashed lines (Ko) show two coalescence models [7]: One where the quarks coalesce as the charm quark with a light di-quark structure and one where all three quarks coalesce. The darker gray band (Greco) indicates a model with three-quark coalescence calculated and diffusion in the hadronic phase [8, 9, 10].

The Λ_c baryons were measured for the first time in heavy-ion–ion collisions [11] at the STAR experiment at RHIC. STAR [12] is a multipurpose experiment with excellent particle identification capabilities that can measure particles at midrapidity in the full azimuth. In particular, the Λ_c measurement was enabled by the Heavy Flavor Tracker (HFT) [13] upgrade that took data in the years 2014–2016. The HFT is a vertex tracker that consists of 4 layers of silicon with a distance-of-closest-approach (DCA) of the tracks to the primary vertex resolution of $\lesssim$30 μm for high-p_T particles. This was allowed by the use of the MAPS technology with excellent granularity for the two innermost layers of the HFT–Pixel detector as well as the small distance from the interaction point.

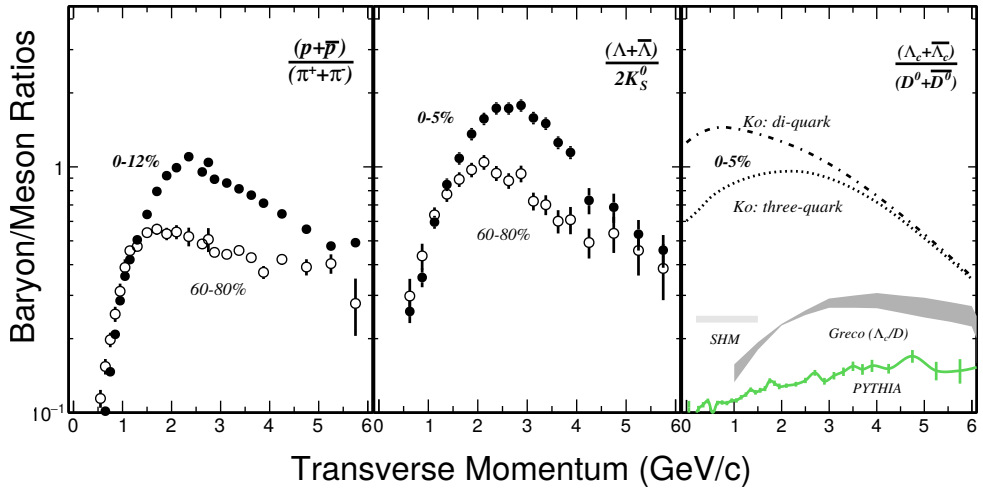

Figure 1: Baryon to meson ratio in RHIC Au+Au collisions with the center of mass energy per nucleon $\sqrt{s_{\mathrm{NN}}} = 200\,\mathrm{GeV}$ vs transverse momentum (p_{T}) [11]. Left: Ratio of the invariant yields of p and $\overline{\mathrm{p}}$ over π^+ and π^- at STAR for the centralities 0–12 % and 60–80 % [3]. Middle: ratio of the yields of Λ over $\mathrm{K}^0_{\mathrm{s}}$ at STAR for central (0–5 %) and peripheral (60–80 %) collisions. Right: Models of ratios of Λ_{c} over D^0 [7, 10, 6].

For the run 2014 data, the cuts for reduction of the background were optimized via the Toolkit for Multivariate Analysis Package [14], using the simulated decayed Λ_{c} particles as signal and background from the measured data. This approach is needed to reduce the background enough to see the peak in the invariant mass spectrum which can be found in Figure 2. A novel data-driven approach to the simulation of the detector effects was developed for the open charm decays at STAR to reduce the computation time and decrease the systematic uncertainties coming from the simulation. Because of the limited statistics in 2014, Λ_{c} were only analyzed in the p_{T} region of 3–6 GeV/c for centralities of 10–60 %.

In this analysis, the efficiency corrections of the yield were done using the data-driven simulations and the systematic uncertainties were obtained by varying the cuts. The ratio of the yields of the Λ_{c} and D^0 was calculated from the published D^0 spectrum [15]. The resulting ratio for p_{T} of 3–6 GeV/c and centrality of 10–60 % was calculated as $N(\Lambda_{\mathrm{c}}^+ + \overline{\Lambda_{\mathrm{c}}^-})/N(\mathrm{D}^0 + \overline{\mathrm{D}^0}) = 1.31 \pm 0.26(\mathrm{stat.}) \pm 0.42(\mathrm{sys.})$. As can be seen in Figure 2, Λ_{c} are clearly enhanced, compared to the D^0. Moreover, the SHM model [6] underpredicts the measured Λ_{c}/D^0 ratio, however more Λ_{c} are produced in the low-p_{T} region where STAR was not sensitive. The data are consistent (within 2σ) with both the di-quark and three-quark coalescence models calculated for the centralities of 0–5 % [7] and are consistent with the "Greco" [10] model calculated for minimum-bias data. Note that the centrality range is different for the the calculations and the data.

As a conclusion, STAR has measured Λ_{c} for the first time in heavy ion–ion collisions thanks to the addition of the HFT in the years 2014–2016. The ratio of the yields of Λ_{c} to D^0 was calculated from the Au+Au data taken in 2014 for centralities of 10–60 %. The results point to an enhancement of the Λ_{c}, that is not consistent with the SHM prediction, but is consistent within 2σ with theoretical calculations that contain quark coalescence.

STAR has recorded approximately twice more data in 2016 compared to the year 2014 with better performance of the HFT. This will allow to measure the ratio of Λ_{c} to D^0 in more centrality and p_{T} bins to put more constrain on theoretical predictions.

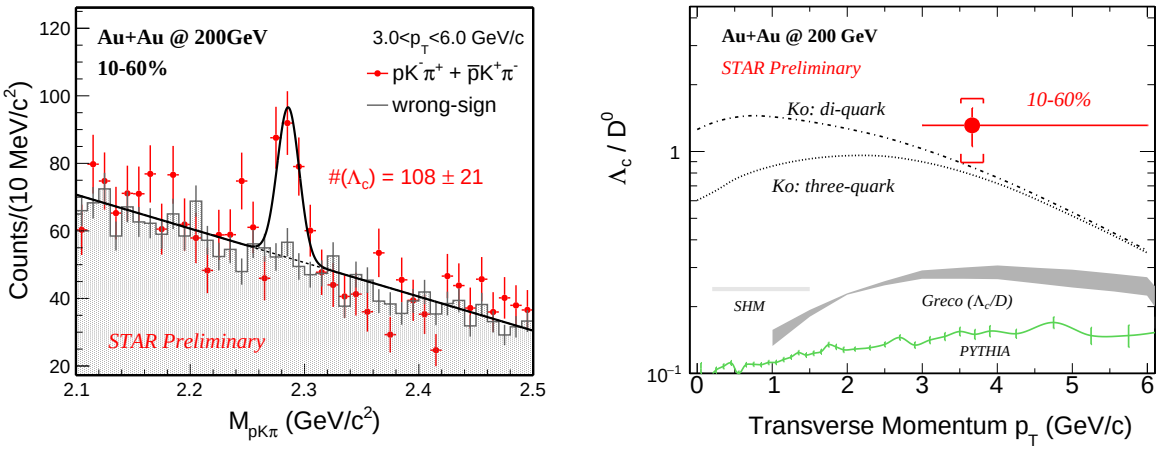

Figure 2: Left: Invariant mass spectrum of the p+K+π triplets in Au+Au collisions with $\sqrt{s_{\mathrm{NN}}} = 200\,\mathrm{GeV}$ at centrality 10–60 % with a transverse momentum cut of $3\,\mathrm{GeV}/c < p_{\mathrm{T}} < 6\,\mathrm{GeV}/c$ [11]. Right: Ratio of the yield of Λ_{c} over D^0 vs p_{T} measured at STAR in Au+Au collisions with centrality 10–60 % [11] compared to coalescence models [7, 10, 6].

Acknowledgements This work has been supported by the grant LG15001 of the Ministry of Education of the Czech Republic.

References

[1] A. Andronic et al. Eur Phys J C 76:107, 2016.

[2] C. Patrignani et al. Chin Phys C40:100001, 2016.

[3] G. Agakishiev et al. Phys Rev Lett 108:072301, 2012.

[4] B. Abelev et al. Phys Rev Lett 111:222301, 2013.

[5] T. Sjöstrand et al. Journal of High Energy Physics 2006:026, 2006.

[6] I. Kuznetsova et al. Eur Phys J C 51(1):113–133, 2007.

[7] Y. Oh et al. Phys Rev C 79:044905, 2009.

[8] V. Greco et al. Physics Letters B 595:202 – 208, 2004.

[9] H. van Hees et al. Phys Rev Lett 100:192301, 2008.

[10] S. Ghosh et al. Phys Rev D 90:054018, 2014.

[11] G. Xie on behalf of the STAR collaboration. Poster and Flash talk: QUARK MATTER XXIV 2017.

[12] K. H. Ackermann, et al. Nucl Inst Meth A 499:624–632, 2003.

[13] J. Kapitán. Eur Phys J C 62:217–221, 2009.

[14] A. Hoecker et al. PoS ACAT:040, 2007. physics/0703039.

[15] L. Adamczyk, et al. Phys Rev Lett 113:142301, 2014.

Evolution of higher moments of multiplicity distribution

Radka Sochorová*(sochorad@fjfi.cvut.cz)*

1 Introduction

Overall observed multiplicity of different types of particles from ultrarelativistic nuclear collisions agrees with the statistical model at temperatures above 160 MeV. The phase transition temperature can be determined by lattice QCD methods as the temperature at which susceptibilities as functions of temperature assume their extremes. This temperature is about 150 MeV. Susceptibilities of different orders manifest themselves in higher moments of the multiplicity distribution. We would like to know how fast different moments of the multiplicity distribution approach their equilibrium value. The evolution of multiplicity distribution out of equilibrium is described by a master equation, which we shall use.

2 Master equation

If we consider a binary process $a_1a_2 \to b_1b_2$ with $a \neq b$, e.g. $\pi N \to K\Lambda$, the master equation for $P_n(\tau)$, the probability of finding n pairs b_1b_2 at time τ has the following form

$$\frac{dP_n}{d\tau} = \epsilon \left[P_{n-1} - P_n\right] - \left[n^2 P_n - (n+1)^2 P_{n+1}\right] \tag{1}$$

where $n = 0, 1, 2, 3...$, $\epsilon = G \left\langle N_{a_1} \right\rangle \left\langle N_{a_2} \right\rangle / L$, $\tau = t\ L/V$ is dimensionless time variable, $V/L = \tau_0^c$ is relaxation time and V is proper volume of the reaction. In eq. (1) for thermal distribution of particle momentum, G is "creation term" and L is "anihilation term". They are thermally averaged cross sections ($G \equiv \langle \sigma_G v \rangle$ and $L \equiv \langle \sigma_L v \rangle$).

2.1 Time evolution of the factorial moments

From the master equation we can get factorial moments.

The scaled 2nd factorial moment is given by $F_2(\tau) = \langle N(N-1) \rangle / \langle N \rangle^2$, the scaled 3rd factorial moment is then $F_3(\tau) = \langle N(N-1)(N-2) \rangle / \langle N \rangle^3$ and the scaled fourth factorial moment has the form $F_4(\tau) = \langle N(N-1)(N-2)(N-3) \rangle / \langle N \rangle^4$. We let the distribution of the multiplicity evolve in time according to the master equation and the result is in the figure 1. For numerical calculations were used binomial initial conditions.

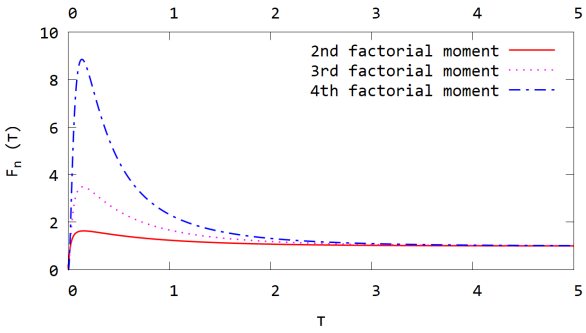

Figure 1: Time evolution of the 2nd, 3rd and 4th factorial moment divided by its equilibrium value for $\epsilon = 0.1$ and $N_0 = 0.005$

3 Real time and temperature dependent master equation

For further study purposes we want to use a master equation that depends on real time. In this case we will calculate the evolution for given chemical species, which appear in the reaction $\pi^+ + n \to K^+ + \Lambda$ with given cross sections. Real time dependent master equation has the form

$$\begin{aligned} \frac{dP_n}{dt}(t/\tau_0^c) = \frac{G}{V} \langle N_{a_1} \rangle \langle N_{a_2} \rangle \left[P_{n-1}(t/\tau_0^c) - P_n(t/\tau_0^c) \right] \\ - \frac{L}{V} \left[n^2 P_n(t/\tau_0^c) - (n+1)^2 P_{n+1}(t/\tau_0^c) \right] . \end{aligned} \tag{2}$$

3.1 Gradual change of temperature

After complete thermalization of the factorial moments, the temperature decreases according to the Bjorken model from the initial temperature $T_0 = 165$ MeV according to the relation

$$T = T_0 \frac{t_0}{t} \tag{3}$$

down to the temperature $T = 100$ MeV, t_0 is hadronisation time for $T = 165$ MeV: $t_0 = 6$ fm/c. We want to obtain the characteristic evolution time of the fireball (around 10 fm/c), so we vary the cross-sections.

3.2 Apparent freeze-out temperature

At the beginning we set the moments to equilibrium values and we let them evolve. Then we are looking for a temperature at which the thermalized system would lead to a given value of the factorial moment in the equilibrium state. From this we are able to determine the apparent freeze-out temperature. This is plotted in the figure 2.

3.3 Central moments

For data processing more important are the central moments, or their combination. Apperent freeze-out temperature for 3rd (left) and 4th (right) central moment for gradual change of temperature is plotted in the figure 3.

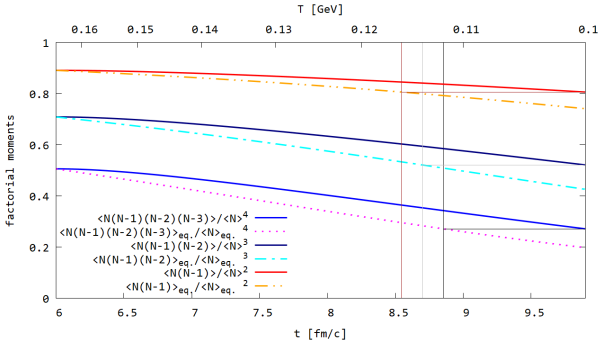

Figure 2: Apparent freeze-out temperature for scaled factorial moments for gradual change of temperature. It is plotted for 15 pions and 10 neutrons and for 200times enlarged cross section.

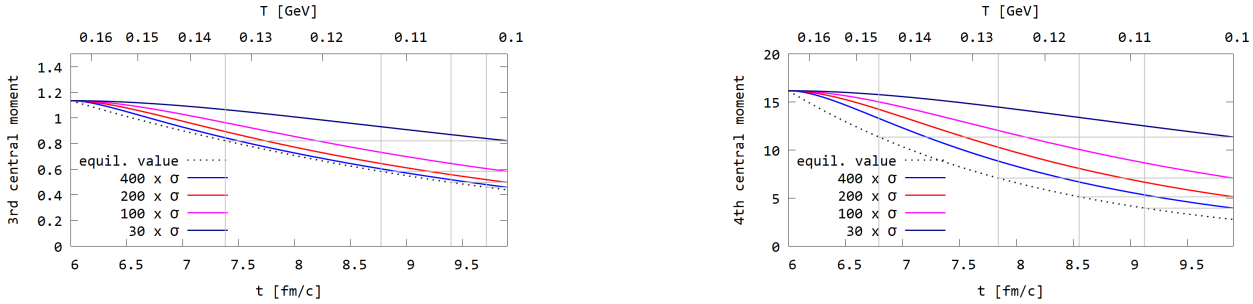

Figure 3: Apparent freeze-out temperature for 3rd (left) and 4th (right) central moment for gradual change of temperature. It is plotted for 15 pions and 10 neutrons and for 200times enlarged cross section.

4 Conclusion

The phase transition temperature can be determined by measuring the higher moments of the proton multiplicity and then comparing with the results for the susceptibilities of the baryon number. Fluctuations in the baryon number usually lead to a seemingly lower phase transition temperature than examining the number of particles. It is perhaps because the higher moments seem to show a different temperature than what we really have. In non-equilibrium state, higher factorial moments differ more from their equilibrium values than the lower moments. The behavior of the combination of the central moments depends on the combination of moments we choose.

References

[1] C. M. Ko, V. Koch, Z.-W. Lin, K. Redlich, M. Stephanov, X.-N. Wang, *Kinetic Equation with Exact Charge Conservation*, Phys. Rev. Lett. **86** (2001) 5438.

[2] PDG: http://pdg.lbl.gov/2016/tables/contents_tables.html [online 17/04/2017].

[3] S. Jeon, V. Koch, K. Redlich, X.-N. Wang, *Fluctuations of rare particles as a measure of chemical equilibration*, Nucl. Phys. A **697** (2002) 546-562.

[4] B. Tomášik and E. E. Kolomeitsev, *Strangeness dynamics in heavy-ion collisions: The K/π ratios and the lifetime of a fireball*, arXiv:nucl-th/0512088v1 (2005).

Cold nuclear matter effects

Jaroslav Štorek*(storejar@fjfi.cvut.cz)*

1 Introduction

Standard Model comprises fundamental particles - quarks, leptons and gauge bosons. Particles made of two quarks are called mesons. If mesons are made of a quark and an antiquark of the same flavour, they are called quarkonia. Quarkonium with a quark b is called an Upsilon Υ.

Firstly, motivation of study and basic terms of high energy nuclear physics will be explained. Secondly, effects of Quark Gluon Plasma (QGP) and Cold Nuclear Matter (CNM) will be described. Finally, some experimental results will be shown.

2 High energy physics

2.1 Motivation

Principal motivation of high energy nuclear physics is to study and understand processes right after collision, when new state of matter, QGP, is created. Side effects, unrelated to the hot QGP phase, called the CNM effects, also occure. It is crucial to distinguish the effects of QGP and CNM in order to learn something about the plasma.

2.2 Basic terms

Centrality of a collision depends on the impact parameter b. For large b, the collision is ultraperipheral and the nuclei do not hit each other. For b similar to the radius of the nuclei, nucleis slightly hit each other, but only few particles are created. For b close to zero, the collision is called central. Central collisions have the highest energy density.

The term pseudorapidity is related to the angle of the emitted particles with respect to the beampipe and describes the range of our detectors.

Due to their large masses, heavy quarkonia belong to 'hard probes', products of large energy transfer interactions in the first moments of a collision. Thanks to their early presence and long lifetimes, we can use them to deduct characteristics of the dense state of matter created in the collision.

Last important term is the nuclear modification factor R_{AA}. R_{AA} is a fraction of a measured yield in nucleus-nucleus collisions and normalised proton-proton collisions. If R_{AA} differs from unity, this is sign of QGP or CNM effects.

3 Effects of QGP and CNM

3.1 Effects of QGP

QGP is a state of matter when quarks and gluons are not bound and can move freely. Now, signatures of QGP will be described.

Thanks to the phenomenon of sequential melting of quarkonia, where different states dissociate under different conditions, the temperature of the QGP medium can be determined.

The phenomena that quarks and gluons can move freely is called asymptotic freedom. This gives rise to the so-called Debye colour screening, where the binding force between the two constituent quarks of a quarkonium system is screened by other gluons and quarks. This happens only when the temperature of collision exceeds the sufficiently high temperature.

3.2 Effects of CNM

Effects of CNM can be observed separately only in collisions with energies insufficient to produce significant amounts of the QGP.

One of the main effects of CNM is nuclear shadowing. Shadowing is result of different parton distribution functions of a nucleon bound in an ultra-relativistic nucleus with respect to free nucleons. This is caused by the different parton densities due to the large Lorentz contraction of the nucleus.

Cronin effect causes that quarkonia in p-p cillisions have generally smaller transversal momentum than that in A-A, because the interacting parton acquires a certain amount of energy by rescattering when going through the nuclear matter.

The most relevant effect for analysis is that about 40% of observed quarkonia Υ(1S) deexcite from states Υ(2S) and Υ(3S). This is called feed-down effect. This needs to be taken into account when interpreting the measured Υ(1S) suppression.

4 Experimental results

Here, we chose some graphs representing interesting effects of CNM.

In Fig. 1, there are data from 200 GeV Au+Au collision by experiment STAR. Y-axis is the ratio of excited states Υ(2S+3S) and Υ(1S) and x-axis is the number of participants. The more participants, the more central collision. The interesting fact about this graph is that in central collisions, Υ(2S+3S) are more suppressed. This is consistent with the phenomenon of sequential melting.

Fig. 2 shows data from 5 TeV p+Pb collision by experiment ALICE. Y-axis describes the nuclear modification factor R_{pPb} and x-axis is the rapidity. Rapidity mainly describes the longitudinal momentum of outcoming particles and is more or less identical to pseudorapidity. Positive rapidity is in the direction of nucleus. In the picture, stronger suppression in forward rapidity than in backward rapidity can be seen, which is interesting and hints at the presence of CNM effects. Coloured lines are suggested models.

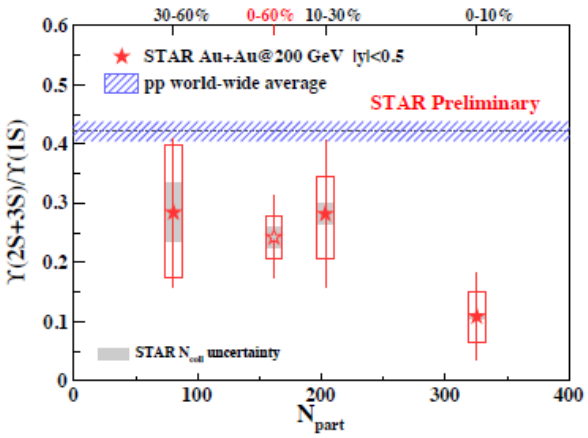

Figure 1: Experimental data from 200 GeV Au+Au collision on experiment STAR. [2]

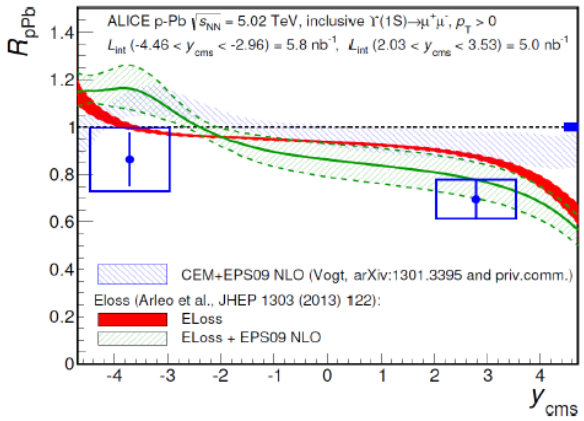

Figure 2: Experimental data from 5 TeV p+Pb collision on experiment ALICE. [3]

References

[1] J. Fodorová: Production of J/Ψ meson in central U+U collisions at the STAR experiment (2016)

[2] Z. Ye: ϒ measurements in p+p, p+Au and Au+Au collisions from the STAR experiment, Quark Matter 2017

[3] I. Das, A. Lardeux: Bottomonium measurements at forward rapidity in Pb-Pb and p-Pb collisions with ALICE, Quark Matter 2017

Optimalization of charm hadrons reconstruction in d/p+Au collisions

Tomáš Truhlář *(truhltom@fjfi.cvut.cz)*

1 Motivation

Charm quark C is created in the beginning of the collision, thus it is quite good tool to study QGP. C is contained in the D mesons e.g. $D^+(c\bar{d}), D^-(d\bar{c}), \ldots$ Our goal is to study $D^0(c\bar{u})$ with decay channel $K^{\pm}\pi^{\mp}$. Nevertheless, the signal from the measurement is strongly suppressed, which makes reconstruction of $D^0(c\bar{u})$ more complicated. The suppression is shown in the Fig. 2, where area of interest can be seen between dashed lines. For this reason, TMVA is used to more efficient signal separation from the background.

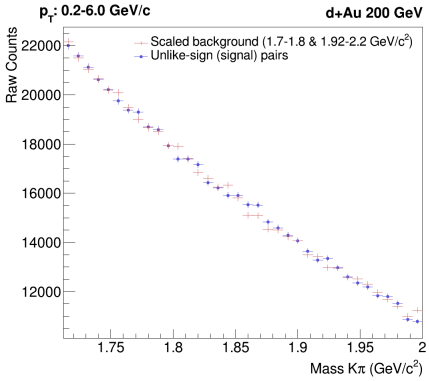

Fig. 1: $K\pi$ unlike-sign pair mass with scaled background.

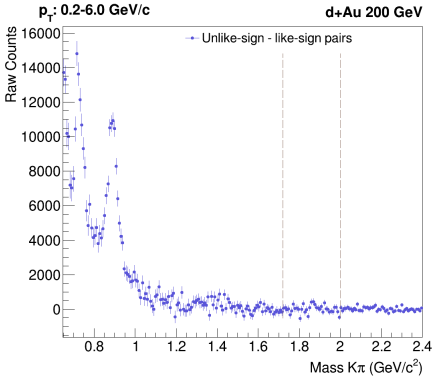

Fig. 2: $K\pi$ unlike-sign pair mass with scaled background subtracted.

2 TMVA

TMVA is shortcut from The Toolkit for Multivariate Analysis[1]. It is package in ROOT containing different multivariate analysis (MVA) methods, e.g.

- Rectangular cut optimization
- Artificial neural networks (ANN, MLP, DNN)
- Boosted/bagged decision trees (BDT)
- ...

2.1 Neural networks

Every method has different implementations e.g. the neural networks, can be implemented as Artificial Neural Network (ANN), Multi-Layer Perceptron (MLP), Deep Neural Network (DNN) or others. TMVA contains only feed-forward neural networks, which means that connections between nodes do not form a cycle. An example of the feed-forward DNN is shown in the Fig. 3. In the example, the DNN is trained to recognize a picture with dimensions two times two pixels and give result of a type of the picture, namely full, vertical, diagonal and horizontal. Each nodes in DNN represent some picture and nodes in the first layer give other nodes an result based on similarity to the picture. The nodes in next layers give an result as sum of all nodes from previous layer weighted over weights. The connection between nodes is represented as colored lines and each color has some weight, the red one have negative weight -1 and black one +1. If there is no line that means that connection weight is 0.

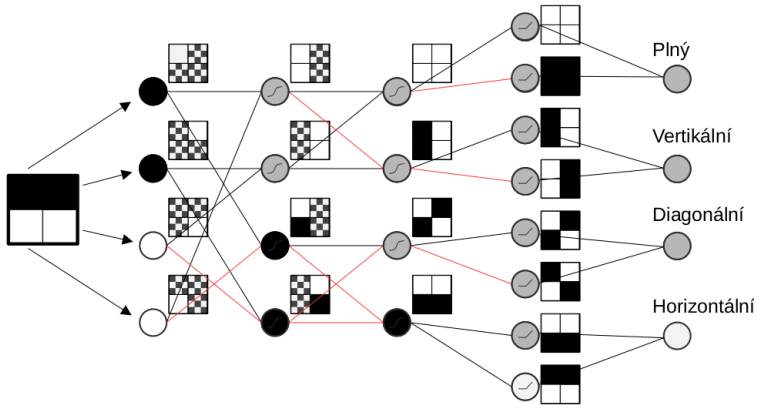

Fig. 3: An example of the feed-forward Deep Neural Network. [2]

2.2 TMVA methods properties

TMVA is a toolkit designed for machine learning applications in high energy physics containing many MVA methods. There is not the best method to use. Each method is designed for different problem. There are many MVA properties: training speed, transparency, performance etc., which help us to choose a suitable MVA method. For example, fast training and transparency methods are useful for solving linear correlations, however, for more complex problem we have to choose method with greater performance, which are more complex with slower training and worse transparency. Background rejection versus signal efficiency is main tool to compare efficiency of different methods and it is shown in the Fig. 4 and 5. According to the second graph if 0,9 signal efficiency is taken then 40 % of background is rejected with BDT, but more than 60 % with DNN.

2.3 TMVA history

TMVA is not new innovation in high energy physics. MVA methods were used in the discovery of the top quark at DØ in 1995. TMVA was created in 2004 and then used at the experiment MiniBooNE, where Boost Decision Trees were used. TMVA was used

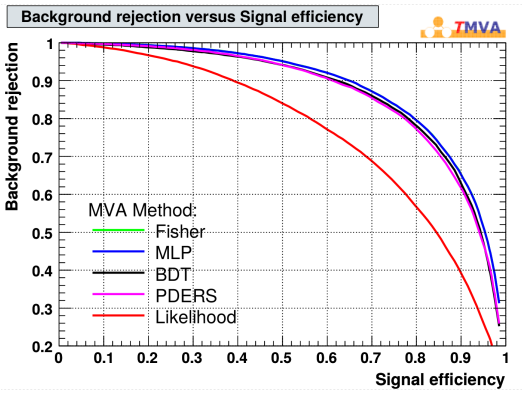

Fig. 4: An example for the background rejection versus signal efficiency for the events of the test sample. [4]

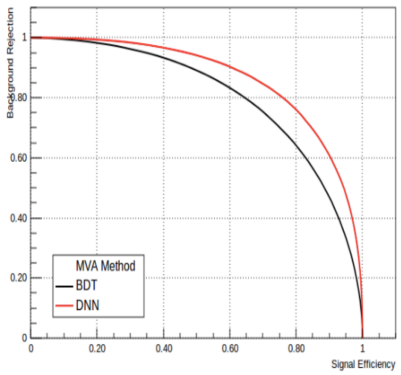

Fig. 5: An example for the background rejection versus signal efficiency for the data from Higgs boson. [3]

in many other experiments e.g discovery of Higgs boson at CMS, reconstruction of Λ_c at STAR and others. Nowadays, TMVA is widely used in high energy physics and it becomes a standard part of many analysis.

3 D^0 reconstruction

TMVA method was used in the D^0 reconstruction, specifically the rectangular cut optimization. And D^0 yield shown in the Fig. 6 was created by our colleague Lian.

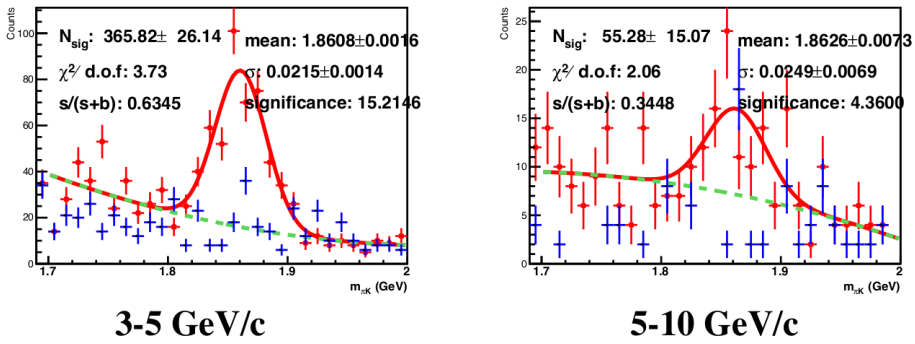

Fig. 6: D^0 yield with 180 M events. Red ones unlike-sign pairs, blue ones like-sign pairs and green ones fitting background. [5]

References

[1] A. Hoecker, *TMVA: Toolkit for Multivariate Data Analysis*

[2] Brandon Rohrer, *How neural networks work*

[3] A Bagoly et al 2017 J. Phys.: Conf. Ser. 898 072046

[4] A. Hoecker et al 2017 arXiv:physics/0703039v5

[5] Liang He, *D0 v2 in Run16 Au+Au 200 GeV*

Multiplicity Fluctuations and Resonances in Heavy Ion Collisions

Josef Uchytil *(uchytjos@fjfi.cvut.cz)*

1 Calculation of the statistical moments within the statistical model

Statistical moments are an important mathematical tool used to describe and calculate multiplicity fluctuations in the statistical model. The m-th central moment $\chi_m(X)$, where $m \in \mathbb{N}$ is defined as follows:

$$\chi_m(X) = E(X - EX)^m$$

where EX is the mean value of the statistical quantity X. We will further concentrate on the first four moments only, as those are of great significance. They are defined and called as follows:

mean: $M = \chi_1$, **variance:** $\sigma^2 = \chi_2$, **skewness:** $S = \chi_3/\chi_2^{3/2}(-3)$, **kurtosis:** $\kappa = \chi_4/\chi_2^2$.

The factor -3 is written in brackets, because it may or may not be included, which depends on whether we want the skewness of the Gauss distribution to be equal to zero. In further calculations, this factor is not accounted for. The meaning of those two moments could be interpreted as follows: skewness measures the assymetry of the probability distribution, kurtosis its "tailedness".

1.1 Grandcanonical and canonical formalism

We usually assume that we work with a grandcanonical or a canonical ensemble, whose event-by-event distributions of conserved quantities are characterized by the moments (M, σ, S, κ) defined above. In order to be able to directly compare theoretical predictions and experimental measurements, we also introduce the so-called *thermodynamic susceptibilities*:

$S\sigma = \chi_3/\chi_2$, $\kappa\sigma^2 = \chi_4/\chi_2$, $M/\sigma^2 = \chi_1/\chi_2$, $S\sigma^3/M = \chi_3/\chi_1$.

The grandcanonical partition (GC) function is given by

$$Z_{GC}(\lambda_j) = \prod_j \exp\left[\sum_{n_j=1}^{+\infty} \frac{z_j(n_j)\lambda_j^{n_j}}{n_j}\right] \tag{1}$$

and the single particle partition function by

$$z_j(n_j) = (\mp 1)^{n_j+1} \frac{g_j V}{2\pi^2 n_j} T m_j^2 K_2\left(\frac{n_j m_j}{T}\right). \tag{2}$$

where

- K_2 is the modified Bessel function, V is the volume of the hadron gas
- $\lambda_j = \exp(\frac{\mu_j}{T})$ is the fugacity for each particle species j
- $m_j$is the hadron mass
- μ_j is the chemical potential of a particle species j
- $g_j = 2J_j + 1$ is the spin degeneracy
- $\mp \ldots$ upper sign for fermions, lower sign for bosons

Canonical formalism is a little more complicated, as it cannot be factorized into one-species expressions, as is the case for the GC formalism. However, we may introduce the Wick-rotated fugacities:

$$\lambda_j = \exp[i \sum_i q_{i,j}\phi_i]$$

and the canonical partition function will now be expressed as:

$$Z_{\vec{Q}} = \left[\prod_{i=1}^{3} \frac{1}{2\pi} \int_0^{2\pi} d\phi_i e^{-iQ_i\phi_i}\right] Z_{GC}(\lambda_j) \tag{3}$$

where Z_{GC} is the GC partition function given by Eq. (**??**).

We will now introduce the vector of total charges

$$\vec{Q} = (Q_1, Q_2, Q_3) = (B, S, Q)$$

and the vector of charges of the hadron species j

$$\vec{q_j} = (q_{1,j}, q_{2,j}, q_{3,j}) = (b_j, s_j, q_j)$$

where Q, B, S denote the charge, the baryon number and the strangeness, respectively.

Furthermore, we cannot take the fact that every hadron species has the same abundance for granted. Let h be a set of hadron species with the corresponding fugacity factor λ_h. We may then write

$$\lambda_j \to \lambda_h \lambda_j$$

and have now everything we need to write down the explicit form of the first four central statistical moments, which is provided in my Research Task.

2 Fluctuations in a hadron resonance gas model with chemical equilibrium

The HRG susceptibilities and the corresponding cummulants can be written in the following form:

- $\chi_l^{(i)} = \frac{\partial^l (P/T)^4}{\partial(\mu_i/T)^l} \mid_T$

- $\chi_1^{(i)} = \frac{1}{VT^3} \langle N_i \rangle_c = \frac{1}{VT^3} \langle N_i \rangle$
- $\chi_2^{(i)} = \frac{1}{VT^3} \langle (\Delta N_i)^2 \rangle_c = \frac{1}{VT^3} \langle (\Delta N_i)^2 \rangle$
- $\chi_3^{(i)} = \frac{1}{VT^3} \langle (\Delta N_i)^3 \rangle_c = \frac{1}{VT^3} \langle (\Delta N_i)^3 \rangle$
- $\chi_4^{(i)} = \frac{1}{VT^3} \langle (\Delta N_i)^4 \rangle_c = \frac{1}{VT^3} \left(\langle (\Delta N_i)^4 \rangle - 3 \langle (\Delta N_i)^2 \rangle^2 \right).$

The equilibrium pressure then reads:

- $P/T^4 = \frac{1}{VT^3} \sum_i \ln Z_{m_i}^{M/B}(V, T, \mu_B, \mu_Q, \mu_S)$
- $\ln Z_{m_i}^{M/B} = \mp \frac{V g_i}{(2\pi)^3} \int d^3k \ln(1 \mp z_i \exp(-\epsilon_i/T))$.

2.1 Inclusion of resonances

The inclusion of resonances can be expressed as follows:

$$VT^3 \frac{\partial(P/T^4)}{\partial(\mu_h/T)}|_T = \langle N_h \rangle + \sum_R \langle N_R \rangle \langle n_h \rangle_R \tag{4}$$

where $\langle N_h \rangle$ and $\langle N_R \rangle$ are the means of the primordial numbers of hadrons and resonances, respectively. The sum runs over all the resonances in the model.

- b_r^R - the branching ratio of the decay-channel and $n_{h,r}^R = 0, 1, \ldots$ - number of hadrons h formed in that specific decay-channel.

There are 26 particle species we consider stable: $\pi^0, \pi^+, \pi^-, K^+, K^-, K^0, \bar{K}_0, \eta$ and $p, d, \lambda^0, \sigma^+, \sigma^0, \sigma^-, \Xi^0, \Xi^-, \Omega^-$ and their respective anti-baryons $\langle n_h \rangle_R \equiv \sum_r b_r^R n_{h,r}^R$.

3 Fluctuations in a hadron resonance gas model without chemical equilibrium

For the sake of brevity, this will be summarized into the following bullet-points:

- **Chemical equilibrium:** $\mu_i = B_i \mu_B + S_i \mu_S + Q_i \mu_Q$,
- **Chemical non-equilibrium:** $\mu_i = \sum_\sigma d_i^\sigma \mu_\sigma$
- d_i^σ - mean number of stable particles emerging in the decay of the level i
- assumption: chemical potential of the mother equal to the sum of the chemical potentials of the daughters
- only configurations for wich the number of particles and antiparticles is the same (e.g. $\mu_N = \mu_{\bar{N}}$.) considered
- SU(3) limit of lattice QCD taken into account - the chemical potentials of the stable **mesons** take a common value μ_π, whereas the stable **baryons** take a value of μ_N
- the equation of state involves only two independent chemical potentials and reads $P = P(T, \mu_\pi, \mu_N)$.

4 Conclusions

We have elaborated and summarized the calculation of the statistical moments within the statistical model as well as ways to compute the multiplicity fluctuations. Furthermore, we have summarized the ways to compute multiplicity fluctuations in a hadron resonance gas model, where a particle production from resonance decays and a thermal equilibrium is assumed. Then the same was performed for the case where no thermal equilibrium is assumed. However, we have discussed the simplified SU(3)-limit-case so far.

In our further work we will aim to generalize the calculations performed for the state of chemical non-equilibrium and compare theoretical predictions to experimental data.

References

[1] W. Florkowski: *Phenomenology of Ultrarelativistic Heavy-Ion Collisions*, World Scientific, Singapore 2010

[2] V. V. Begun et al.: *Multiplicity fluctuations in hadron resonance gas*, Phys. Rev. C **74** (2006) 044903

[3] P. Alba, *et al.*: *Sensitivity of multiplicity fluctuations to freeze-out conditions in heavy ion collisions*, Phys. Rev. C **92** (2015) 064910

[4] G. Torrieri, J. Letessier, J. Rafelski: *SHAREv2: Fluctuations and comprehensive treatment of decay feed-down*, Comput. Phys. Commun. **175** (2006) 635

[5] G. Torrieri, S. Jeon, J. Rafelski: *Particle yield fluctuations and chemical nonequilibrium in Au+Au collisions at* $s_{NN}^{1/2} = 200\ GeV$, Phys. Rev. C **74** (2006) 024901

[6] H. Bebie, P. Gerber, J. L. Goity, H. Leutwyler: *The role of the entropy in an expanding hadronic gas*, Nucl. Phys. B378 (1992) 95

[7] F. Becattini et al.: *Multiplicity fluctuations in the hadron gas with exact conservation laws*, arXiv:nucl-th/0507039v1, 14 Jul 2005

[8] M. Nahrgang et al.: *Impact of resonance regeneration and decay on the net proton fluctuations in a hadron resonance gas*, Eur. Phys. J. C(2015) 75:573, DOI 10.1140/epjc/s10052-015-3775-0, 1 Dec 2015

[9] J. Fu: *Higher moments of net-proton multiplicity distributions in heavy ion collisions at chemical freeze-out*, Phys. Let. B 722 (2013) 144-150, 9 Apr 2013

[10] F. Karsch, K. Redlich: *Probing freeze-out conditions in heavy ion collisions with moments of charge fluctuations*, arXiv:1007.2581v1 [hep-ph], 15 Jul 2010

[11] M. Kitazawa, M. Asakawa: *Revealing baryon number fluctuations from proton number fluctuations in relativistic heavy ion collisions*, arXiv:1107.2755v2 [nucl-th], 2 Mar 2012

[12] L. Adamczyk et al.: *Energy Dependence of Moments of Net-proton Multiplicity Distributions at RHIC*, arXiv:1309.5681v1 [nucl-ex], 23 Sep 2013

[13] M. Kitazawa, M. Asakawa: *Relation between baryon number fluctuations and experimentally observed proton number fluctuations in relativistic heavy ion collisions*, arXiv:1205.3292v1 [nucl-th], 15 May 2012

[14] X. Luo: *Error Estimation for Moments Analysis in Heavy Ion Collision Experiment*, arXiv:1109.0593v2 [physics.data-an], 2 Nov 2016

Simulation of semiconductor pixel detector response

Matěj Vaculčiak*(vaculmat@fjfi.cvut.cz)*

1 Introduction

The thesis aims to find an optimal geometric layout of SpacePix detector, which is currently being developed at FNSPE to measure cosmic radiation beyond low Earth orbit. Particles expected to be detected are of two types. Those have their source at Van Allen radiation belts and galactic cosmic rays with higher energies such as 55Fe isotopes.

2 Semiconductor detectors

SpacePix is planned to be a semiconductor pixel detector, so the principles of semiconductor particle measurements should be mentioned.

2.1 Semiconductor materials

Materials can be described with band structure, which is a discrete energy spectrum of electrons. Based on the band-gap size materials can be generally classified as conductors, semiconductors or insulators (see 1). For a particle detection semiconductors, particulary P and N, are important. Semiconductors are generaly materials with band gap size smaller than 3 eV being therefore capable of current conduction at specific circumstances. P and N-type semiconductors are created by doping a material with atoms of an element with slightly different proton number, e.g. doping silicon with arsenic. It results in an addition of free charge carriers, positive or negative, based on dopant type, creating P or N semiconductor.

2.2 Depletion zone

When connecting a junction of P and N semiconductors to a bias voltage a so-called depletion zone is created. It means that the majority of the free charge carriers moves away from the junction, leaving the area electrically neutral. The depletion zone is key for particle detection because as the charged particle traverses this area it ionizes bound electrons setting them free and creating electron-hole pairs. These objects drift in the electric field caused by bias voltage through the material and when they reach a sensor signal is obtained [2]

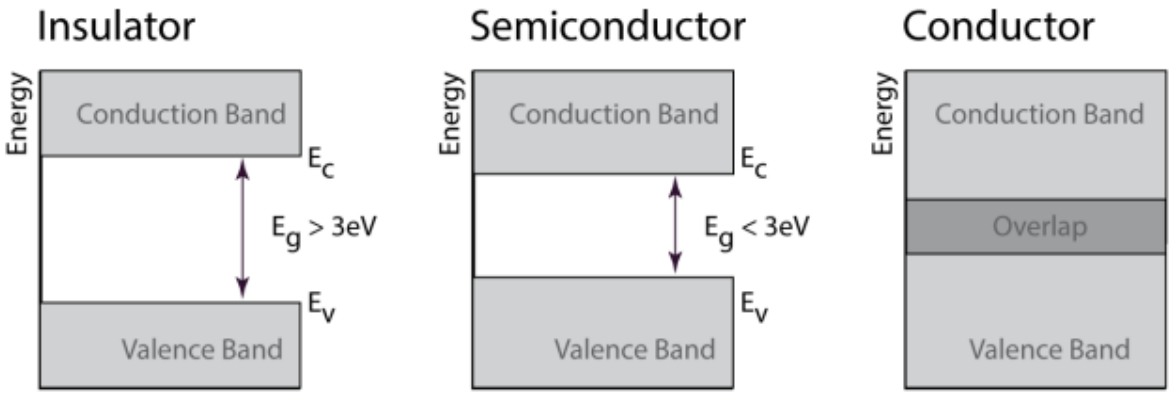

Figure 1: Band structure model, [1]

3 Detector simulation

Simulations were executed in order to suggest an optimal geometric layout based on e.g. a size of clusters created by incoming particles or Bragg peak position.

3.1 Geant4

For SpacePix the Geant4 was used. It is a worldwide used particle-through-matter simulation toolkit containing a set of C++ libraries. When a virtual particle traverses material, Monte Carlo methods are used to decide which physical actions take effect. These actions are given via physics lists, registers of actions corresponding to particular physics phenomenon. This aspect of Geant4 is very useful as it allows the user only to pick a restricted area of physics to be taken into account (e.g. excluding hadronic physics when simulating electrons), making the simulation much less processor-time consuming. Another advantage of Geant4 is the ability to create objects with various geometric layouts.

4 Conclusion

The thesis focuses on Geant4 simulations execution in order to obtain data needed for SpacePix chip development. Unfortunately, until the WEJCF not many data were simulated, except the position of Bragg peak, which was crucial for lab measurements conduction, so any interesting results could not be presented.

References

[1] Havránek, M., 2017, *Silicon sensors of ionizing radiation.* [pdf], FNSPE CTU. Available at: < http://aldebaran.cz/ havranek/EMJF/01_sensors.pdf> [Accessed 29 November 2017]

[2] Knoll, G. F., 2010, *Radiation detection and measurement.*, 4th ed.1, Wiley

Study of $D^{\pm}$ in Au+Au collisions at $\sqrt{s_{NN}} = 200$ GeV at the STAR experiment

Jan Vaněk *(vanek@ujf.cas.cz)*

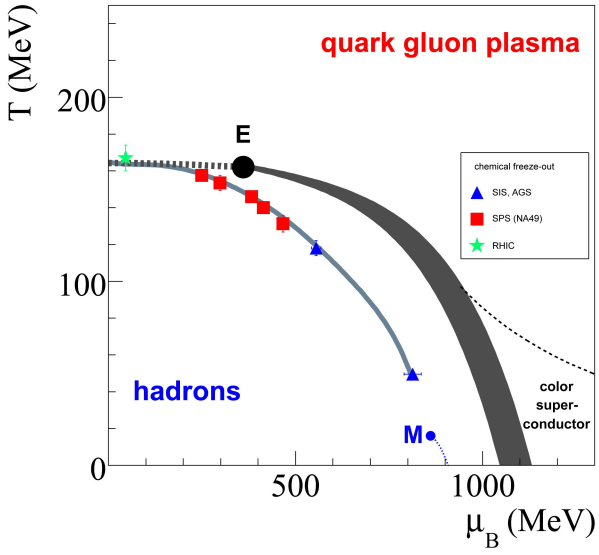

Figure 1: Phase diagram of nuclear matter. On the y axis there is temperature T and on the x axis there is baryon-chemical potential μ_B. The shaded area represents anticipated first order transition, the dashed line at low μ_B is cross-over transition and E is critical point. Point M marks state of nuclear matter present inside atomic nuclei and the remaining points represent place of chemical freeze-out calculated from statistical model. Individual phases of nuclear matter are denoted in the plot. Taken from Ref. [1].

One of the main goals of heavy-ion programme at the STAR experiment is study of the phase diagram of nuclear matter. Example of the diagram is shown in Fig. 1. The Lattice-QCD, in a simple model, predicts three phases of the nuclear matter. At low baryon-chemical potential μ_B and low temperature T is the hadronic phase where quarks and gluons are trapped inside colorless hadrons which is the phase observed in the surrounding universe. At hight μ_B and low T lies the color super-conductor. This phase is currently just hypothetical and has not been observed yet. And finally, at high T lies the quark-gluon plasma (QGP) where the quarks and gluons are no longer confined inside hadrons. The model also predicts the types of the phase transitions. At low μ_B there should be a cross-over phase transition at critical temperature $T_c \approx 170$ MeV (dashed line

in Fig. 1) and at higher μ_B there should be a first order transition (gray band in Fig. 1). This structure also implies existence of a critical point E.

The ultra-relativistic heavy-ion collisions provide access to the low-μ_B, high-T region of the phase diagram and so to the QGP. Such collision has quite complex time evolution as shown in Fig. 2. The first stage of the collision is called the hard scattering when the partons collide with each other. In this phase, most of the high energy and heavy quarks and gluons is created. Approximately 1 fm after the hard scattering, the QGP fire-ball is ignited. The medium then expands and its temperature decreases until it reaches critical temperature T_c. At that moment, the quarks and gluons are no longer asymptotically free but are confined inside hadrons which can change species and interact with each other. The expansion and temperature drop proceeds. When temperature of chemical freeze-out T_{ch} is reached, the hadrons can still interact, but they do not change species. The hadronization process is complete when kinetic freeze-out temperature T_{fo} is reached. From that moment on, the hadrons do not change species and do not interact. This is the final state of the collision which is observed by detectors at colliders.

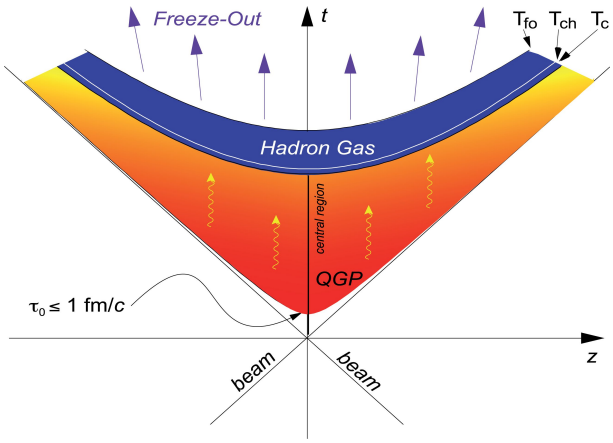

Figure 2: Diagram of the time evolution of a heavy-ion collision, where z is the beam axis, t is time, T_c is critical temperature, T_{ch} is temperature of chemical freeze-out and T_{fo} is temperature of kinetic freeze-out. For more detailed description see the text. Taken from Ref. [1].

As a probe to the QGP, quarks and gluon from the hard scattering are used. As mentioned above, they are created before the QGP ignition, therefore they have to pass through the medium where they loose energy and momentum. This phenomenon can be quantified using the nuclear modification factor R_{AA} which can be defined as

$$R_{AA}(p_T) = \frac{\frac{dN_{AA}}{dp_T}}{\langle N_{coll} \rangle \frac{dN_{pp}}{dp_T}} \tag{1}$$

where the numerator is particle multiplicity in heavy-ion collision (A-A coll.) and the denominator is particle multiplicity in proton-proton collision (p-p coll.) scaled by mean number of binary collisions $\langle N_{coll} \rangle$. If the heavy-ion collisions were just simple superposition of p-p collisions, the R_{AA} would be equal to unity. This is not true as verified by experiments at the Relativistic Heavy-Ion Collider (RHIC) in Brookhaven National Laboratory and the Large Hadron Collider (LHC) in CERN.

The main goal of this analysis is to compute the R_{AA} of $D^{\pm}$ mesons in Au+Au collisions at $\sqrt{s_{NN}} = 200\,\text{GeV}$ measured by the STAR experiment in 2016. Precise topological

reconstruction of $D^{\pm} \rightarrow K^{\mp} + \pi^{\pm} + \pi^{\pm}$ is used and is enabled by the STAR Heavy Flavor Tracker (HFT). An extensive study of STAR detector acceptance and efficiency will be carried out in order to correct the $D^{\pm}$ invariant yield spectra. Poster with the preliminary results of this analysis is to be presented on Quark Matter 2018 conference.

References

[1] M. Kliemant, *et al.*, Lect. Notes Phys.785 (2010) 23.

Study of Rydberg atom trapping and manipulation using magnetic fields

Alena Zemanová*(zemanal5@fjfi.cvut.cz)*

1 Rydberg atoms

Rydberg atoms are atoms, in which at least one electron is excited to a high quantum state. Ground states of atoms have principal quantum number n from 1 to 7, whereas Rydberg states has n as big as e.g. 300. Due to large distance between the electron and the ion-core an extremely large electric dipole moment (d) is possible, so these atoms have an exaggerated response to electric and magnetic fields, which can be used for manipulating them in external fields.

2 Experiment AEgIS

2.1 Overview

One of the experiments that use Rydberg atoms is experiment AEgIS (Antihydrogen Experiment: Gravity, Interferometry, and Spectroscopy). This experiment is located in CERN and its aim is to perform a direct test of the universality of the free-fall on a beam of cold antihydrogen.

The experiment works in eight simple steps. At first, positrons are produced by a ^{22}Na source and cooled down in Surko trap. Positrons are then captured and accumulated in an accumulator. Nowadays, more than 3000 pulses from the Surko trap can be stored during 15 minutes.

Next step is the production of positronium (Ps). The Ps formation mechanism chosen by AEgIS uses a semiconductor converter where positrons are implanted at about keV energy in the surface. Last part concerning positronium is its excitation to a high Rydberg state by laser excitation by a group of lasers whose wavelengths were tuned in the range 204-206 nm for first step ($n = 3$), and 1680-1715 nm for second step ($n = 15 - 17$).

After that, antihydrogen is finally pulsed-formed by resonant charge exchange between Rydberg Ps and cold antiprotons. This step is the last one in the current experimental setup.

Next two steps should be installed in the experiment during the next 5 years. The first one is the formation of antihydrogen beam by Stark acceleration and the second one is finally measurement the g in a two-grating Moiré deflectometer coupled with a position-sensitive detector.

2.2 Layout of the experiment

From the hardware point of view, AEgIS is a complex system built around its principal vacuum chamber (see Figure **??**). The positron system consists of Surko trap, positron accumulator and vacuum test chamber that is located above principal vacuum chamber. From this part of the experiment leads a magnetic transfer for positrons to the main part of the setup. The principal vacuum chamber is divided into two parts with different magnetic fields: a 4,43 T region, which is used for antiproton cooling and 1 T region for antihydrogen formation. Both regions have the Penning-Malmberg traps, so the storage and manipulation of atoms in a high magnetic field is possible.[**?**]

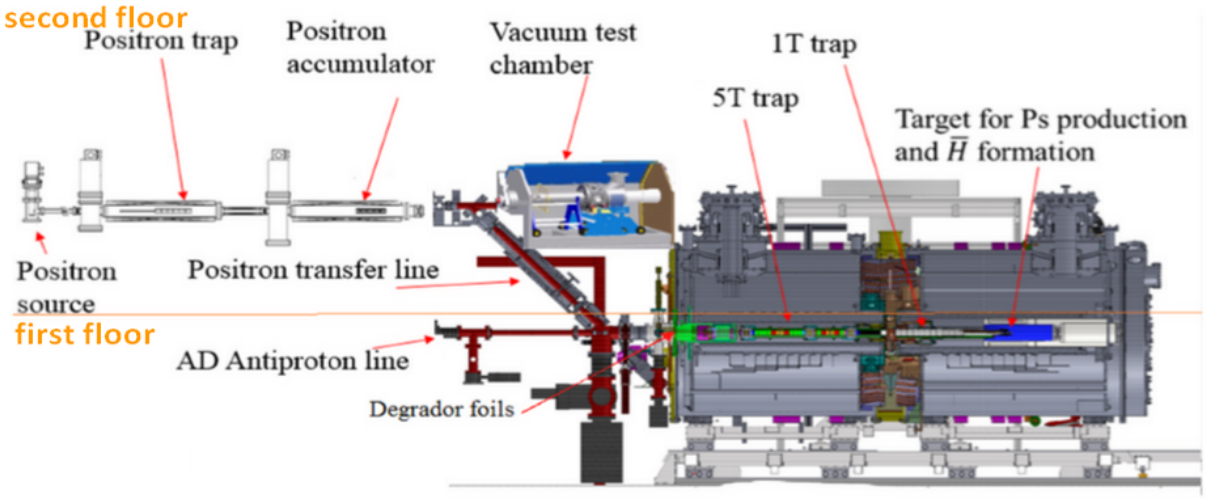

Figure 1: Experimental setup. [**?**]

3 Manipulation and trapping Rydberg atoms in magnetic field

The secondary goal of the experiment AEgIS is to carry out spectroscopic measurements on antihydrogen atoms, so the trapping of these atoms would be very useful and needed. The motion of antihydrogen atoms in electric and magnetic fields of arbitrary orientation was studied by M. Špaček and V. Petráček and presented in [**?**]. The aim of their work was to find an exact model of external and internal dynamics. Finally, an expression for the force acting on an antihydrogen atom in an arbitrary field was derived. The general formula for this force can be seen in [**?**].

Following this some simulations of motion of antihydrogen atoms in magnetic field was made. The map of the field was taken directly from experiment AEgIS, that means the map follows 4,46 T and 1 T region described above. The line between these two regions is placed at zero.

The main result of this simulation can be seen in the Figure **??**. In the upper part of the figure the velocity of atoms and in the lower part the position of atoms is plotted. The figure shows a stable orbit of antihydrogen atoms with initial velocity $\vec{v} = (0,001; 0; 350)$cm/s and initial position $\vec{x} = (0, 0, 0)$cm. New quantum numbers n_A and n_B (described in [**?**])

are varied. It can be seen in the figure **??** that for low velocities of atoms (temperature about 10 mK) a stable orbit can be found, atoms can be trapped and moreover, they can accelerate themselves to velocity about 1400 cm/s.

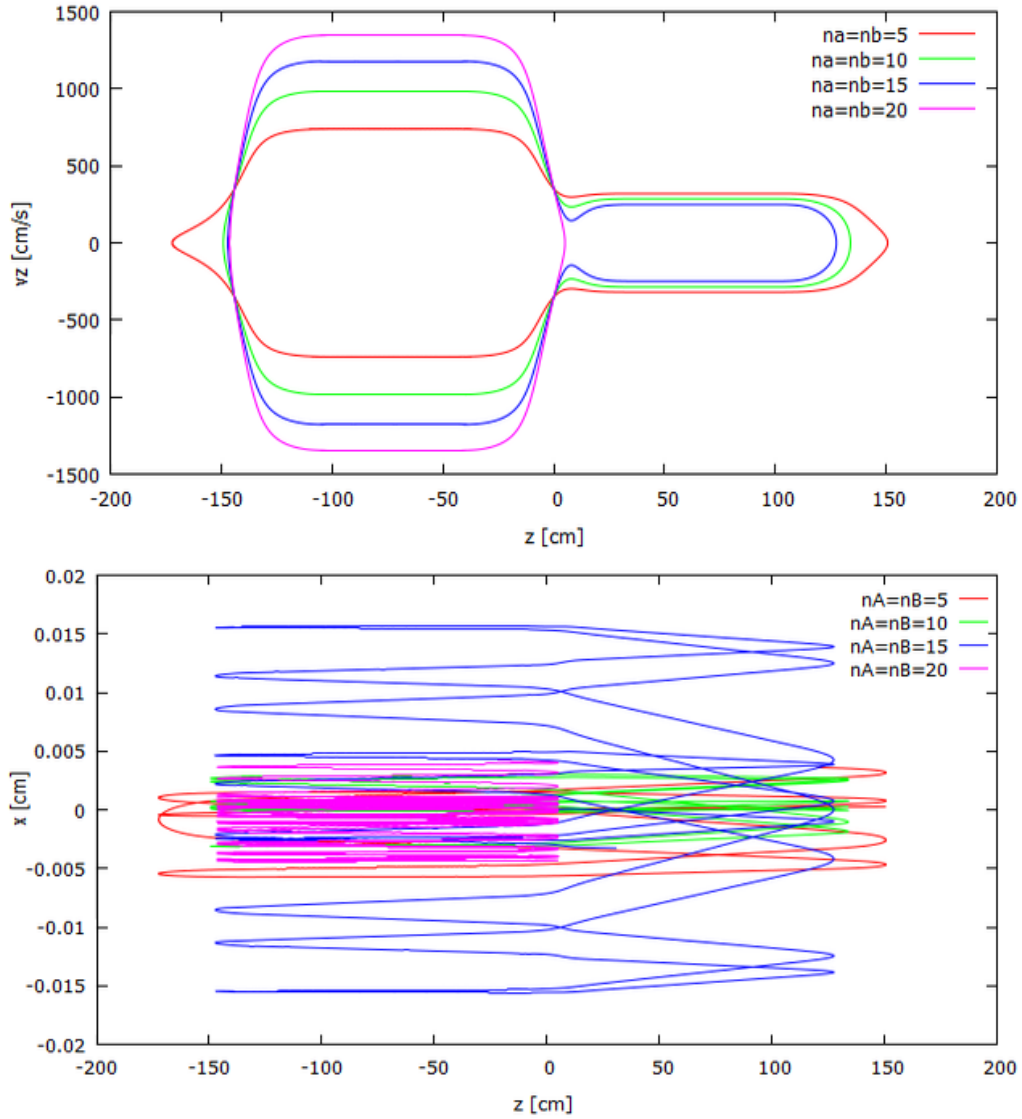

Figure 2: Velocity (top) a trajectory (down) of atoms for different $n_A = n_B$. Initial conditions: $\vec{x} = (0; 0; 0)$ cm, $\vec{v} = (0,001; 0; 350)$ cm/s.

References

[1] Pauline Yzombard: *Laser cooling and manipulation of Antimatter in the AEgIS experiment*. Ph.D. Thesis, 2016.

[2] M. Špaček, V. Petráček: *Internal and external dynamics of antihydrogen in electric and magnetics fields of arbitrary orientation*, 21.6.2012 . `https://arxiv.org/pdf/1206.5171.pdf` [online 1/3/2018]

Investigation of the theoretical uncertainties in the jet production kinematics

Vladimír Žitka*(zitkavla@fjfi.cvut.cz)*

One of the sources of theoretical uncertainties in the jet production predictions is the value of the strong coupling constant α_S. It is therefore important to understand what the strong coupling is and how it can be measured.

1 Properties of α_S

The strong coupling is a property of standard model that characterizes the relative strength of QCD in relation to the other interactions. It is similar in this respect to the fine structure constant α for electro-magnetic interaction. The important difference between the two constants is that α_S is not constant. This property is often called running coupling. In predictions made by using perturbative QCD(pQCD) values of observables are expressed in terms of the renormalised coupling $\alpha_S(\mu_R)$, which is a function of a renormalization scale μ_R. The running coupling is defined by the renormalization group equation[1]:

$$\mu_R^2 \frac{d\alpha_S}{d\mu_R^2} = \beta(\alpha_S) = -(b_0\alpha_S^2 + b_1\alpha_S^3 + b_2\alpha_S^4 + \dots), \tag{1}$$

where the b_i are the i-loop β-function coefficients. The values of the first few relevant loop coefficients are: $b_0 = \frac{33-2n_f}{12\pi}$, $b_1 = \frac{153-19n_f}{24\pi^2}$ and $b_2 = \frac{2857-\frac{5033}{9}n_f+\frac{325}{27}n_f^2}{128\pi^3}$. The n_f in loop coefficients is the number of quark flavours which are considered light ($m_q \ll \mu_R$). It is an expression of the relationship between strong coupling and the effective theory that is employed in predictions. Furthermore, the minus sign in equation (1) can be interpreted as the origin of asymptotic freedom - the well known fact that the strong interaction withers for processes involving large momentum transfers (the so called hard processes) and inversely burgeons for scales below 1 GeV. One of the challenges in determining the value of α_S is the fact, that different measuring methods result in different values. This is demonstrated in Fig.1. The reference value is always taken to be the value of α_S for renormalization scale equal to the mass of the Z boson.

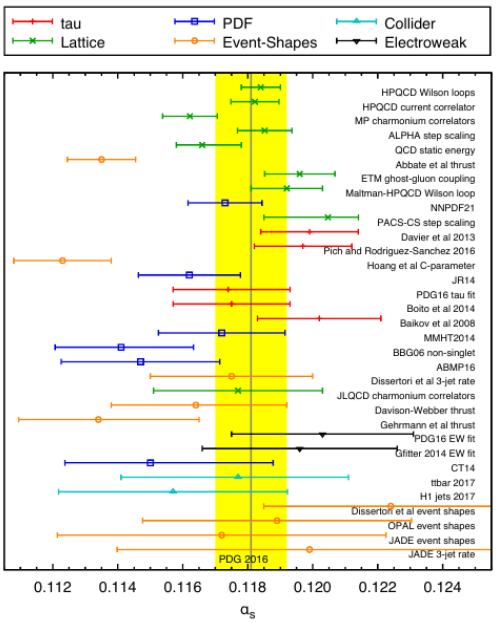

Figure 1: The world average of α_S values acquired using different measuring methods as compiled by [2].

2 How to measure α_S

The simplest way to determine the value of strong coupling is from the ratio of two- and three-jet events that result from annihilation of electron and positron. This is the purest case due to the fact that there are no strongly interacting objects and therefore all the strong interaction occurs in the final state only. Moreover, the probability of emission of additional quark or gluon in the final state is proportional to the value of α_S.
Another feasible approach is to examine the shapes of measurable quantities such as the transverse momentum spectrum of particle jets, the azimuthal separation of the two leading jets in event.

3 Simulations

The approach employed in current study is the second one. The current situation is that sufficient bulk of simulated data is being assembled using the Pythia 8. The matrix element for pQCD generation of proton proton collisions is QCD 2 to 2. The simulated collisions have $\sqrt{s} = 13$ TeV and the PDF set used was default CTEQ 5L LO. It is possible to vary the value of α_S for different parts of generation in Pythia. The varied values are put into the cross section of the generation, timelike showering, spacelike showering and MPI. Variation to the day of presentation has been for $\alpha_S \in (0.060, 0.180)$ with the step of 0.02. The final step in generation is the reconstruction of particle jets in events. That is done using the Anti-k_t algorithm with the radius parameter $R = 0.4$. The reconstructed jets are then subject to cuts on transverse momentum and rapidity: $p_T > 150$ GeV and $|y| < 4.8$.
One of the final goals of this research project is to find and investigate the variable that is the most responsive to the variation of α_S. However, the work shown here is only a

work in progress that includes an example of the influence of variation on the shape of the azimuthal separation of two leading jets in event. This variable is selected because it is sensitive to the shape of the event rather than jet energy scale or resolution. If there were only two jets in each event the azimuthal separation would have a unambiguous peak in π. As that is not the case the spectrum rises towards π. The more jets there are in an event the lesser is the azimuthal separation between the leading two, simply because the 4-momentum has to be conserved. An example can be seen in Fig.2, the event has been selected if it contained at least two jets.

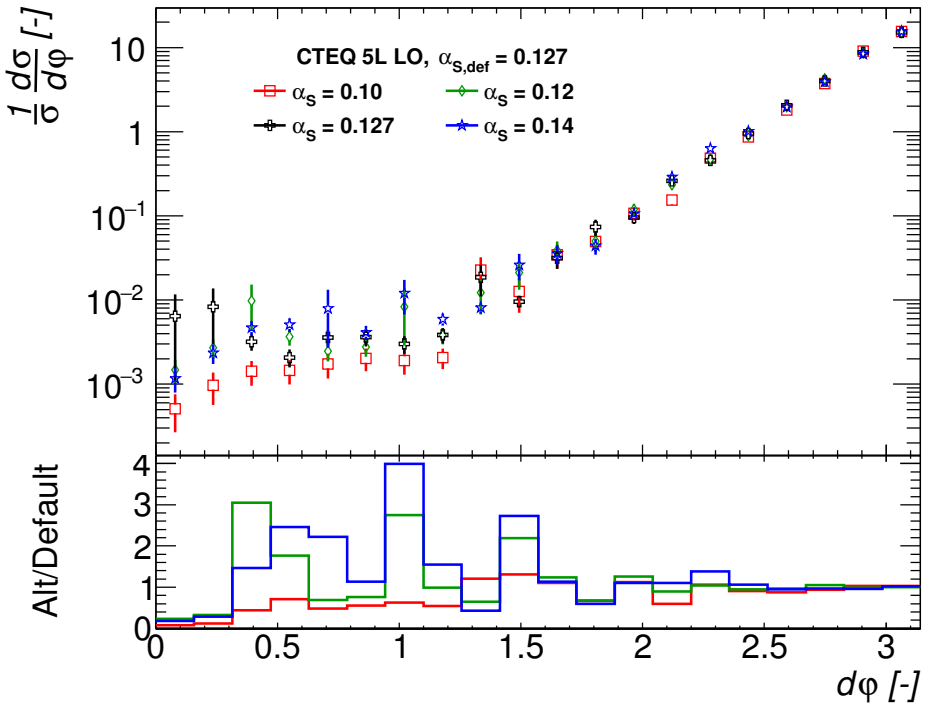

Figure 2: The azimuthal separation of the leading two jets in event.

It can be seen that for higher value (blue line) of α_S there is a hint of enhancement of the lowest part of the spectrum against the lower value (red line). The significance of this enhancement however remains to be determined and is one of the goals of future studies along with more precise study of other measurables.

References

[1] C. Patrignani et al. Review of Particle Physics. *Chin. Phys.*, C40(10):100001, 2016.

[2] G. P. Salam. The strong coupling: a theoretical perspective. 2017.